ISSN: 2754-4915

Journal of Material Sciences & Manufacturing Research

SCIENTIFIC Research and Community

Review Article

Open Access

Crystalline Phase Change Due to High-Speed Impact on Steel

Muna Slewa

Embry–Riddle Aeronautical University, Prescott, AZ, USA

ABSTRACT

Standard alloy steels have many industrial applications because they are easily machined and welded. The alloy contains less than 0.3% carbon by weight and is considered a low-carbon alloy. Because of this low carbon content, the alloy is helpful as a general-purpose steel. It is extreme, tough, ductile, weldable, and malleable. It is used to build bridges, buildings, cars, heavy equipment, and the construction industry. A36 steel contains small elements, including manganese, sulfur, phosphorous, and silicon. so, these elements give the alloy steel the desired mechanical and chemical properties. The steel alloy A36 gets the number 36 on its name due to its yield strength. Steel has a minimum strength of 36,000 pounds per square inch. However, the effect of impact at high velocity on the crystalline structure and phase material is unspecified and the aim of this study.

The physical properties and molecular structure of steel from the effect of high velocity on grain structure and unknown properties are being studied in this research. The primary measure of the impact changes in the interconnected mineral crystal structure at various locations around the impact crater. The effect of super-projectile velocity on the crystalline grain structure near the target effect in almost all formations. This strength shows high some sites at all post-impact stages. This study also found that the crystal structure of BCC remained the dominant phase after impact. This result is realistic with all test samples and all levels of shock loading.

A36 steel has been studied and is predominantly a single- phase body-focused cubic (BCC) material. Impact speeds ranged between 3.54 and 6.70 km/s. Target subjects before and after impact were reviewed to determine if ductility in the material. The physical properties and molecular structure of A36 steel are also known.

Portions were cut from approximately 90 x 90 square microns of test samples, in line with standards required for surface finish. These surfaces were examined and analyzed after impact. The surface portions were selected from a range of areas, including areas directly below the impact crater, to sites that were not physically affected by the impact. Three different effect speeds were applied, and the prepared samples were examined. An EBSD (Electron Backscatter Deflection) imaging microscope is used to examine the crystal structure of the test specimen after impact.
Most minerals crystallize into one of three predominant structures: body-centered cubic (BCC), hexagonal closely packed cubic (HCP), or face- centered cubic (FCC). Since these crystal structures are the most predicted lattice configurations, postimpact samples are examined for changes in molecular structure assignment. The results were then tabulated according to the relative impact pit in the region. Previous research shows that post-impact inspection of HCP phase change, in iron specifically, can be entirely and rapidly reversed during impact.

However, in this study, traces of HCP were found at impact conditions led to a change in the A36 phase. The methods of electron microscopy, surveying electron back diffraction and X-ray of distortions, lattice defects, twinning, and phase shift were investigated. A limited number of targets were affected. 304L and HY100 were also examined. These alloy steels contain a BCC crystal phase and face-centered (FCC) hexagonal closed beam (HCP) structures. The grain size is close as well. The impact is compressed close to the impact site. Also, the twinning was located closer to the impact zone and gradually dissipated away from the impact zone. In contrast, the increase of the effect's momentum increased the percentage of HCP.

***Corresponding author**

Muna Slewa, Embry–Riddle Aeronautical University, Prescott, AZ, USA.

Received: March 25, 2025; **Accepted:** March 28, 2025; **Published:** May 09, 2025

Introduction

A36 Steel

High-velocity impact on metals often causes surface damage and permanent deformation. Such effects can be viewed by the naked eye. We examine here what the high-speed impact will have on the inevitable phase change of the crystalline structure, let alone the atomic reorganization, because of the impact on the A36 steel. On the crystalline and atomic level, this can only, be detected by the Electronic Spectral Microscope (ESM). A36 steel is a standard steel alloy that has many global applications.

The physical characteristics and molecular structure of A36 steel are well known. The effects of high-speed velocity impact on the crystalline structure and material phase changes due to impacts are studied herein experimentally. Evidence of microstructural phase transition and modifications has been identified by Backscatter Diffraction and Transition Electron Microscopy. According to Hixon, Gray and Dougherty, scientists discovered that body-centered cubic (BCC) alpha-iron (α) undergoes a fully reversible phase transition to Hexagonal Close Packed (HCP) epsilon-iron (ε) at room temperature and 13.00 GPa [1-3]. The effects of an impact on the crystalline structure are assessed by impacting A36

steel plates (15.4 x 15.4 x1.27 cm) with Lexan projectiles. A two-stage light gas gun accelerates these projectiles to velocities of 3-6 km/s at the point of the impact. The surfaces of the impacted plates are prepared as required for inspection by the Electron Back Scatter Diffraction (EBSD) microscope. Ten regions on each impacted plate area are examined. Each region is approximately (90x90) square microns. These regions are distributed from the area immediately under the impact crater to locations that are not physically affected by the impact. In this first phase, we examined a sample impacted at 3.54, 4.51, and 5.80 km/s. Observations of collected EBSD images show that the predominant phase is Body-Centered Cubic (BCC). Face-Centered Cubic (FCC) and Hexagonal-Close-Packed (HCP) phases are also indexed.

304L Steel

High yield 304L steel is a unique alloy known for its employment in construction and has many global applications. The quenched and tempered low carbon 304L stainless steel plate has a minimum tensile strength of 70 ksi and a yield strength of 0.2% of 25 ksi [1]. It also provides good ductility, first-class toughness, corrosion resistance, and weldability. Traces of Chromium and Nickel in 304L give it the desired corrosion resistance properties. These properties make 304L an ideal candidate for applications in pressure vessels and petrochemical industries. High-velocity impact on metals often causes surface damage and permanent deformation. The Electronic Spectral Microscope (ESM) can only detect the effects on the crystalline and atomic levels.

The physical characteristics and molecular structure of 304L steel are well known. Backscatter Diffraction and Transition Electron Microscopy have identified evidence of microstructural phase transition and modifications. Hixon, Gray, and Dougherty [4-6], discovered that body-centered cubic (BCC) alpha-iron (α) undergoes a fully reversible phase transition to Hexagonal Close Packed (HCP) epsilon-iron (ε) at room temperature and 13.00 GPa.

The effects of high-speed velocity impact on the crystalline structure and material phase changes are studied herein experimentally. The high-speed impact on the crystalline structure's inevitable phase change is examined, let alone the atomic reorganization resulting from the impact on the 304L steel. The effects of an impact on the crystalline structure are assessed by impacting 304L steel plates same dimensions of A36 steel with Lexan projectiles. A two-stage light gas gun accelerates these projectiles to a velocity of 6.70 km/sec at the point of the impact. The impacted plates' surfaces are prepared for the Electron Back Scatter Diffraction (EBSD) microscope inspection [7,8]. Nine regions on each impacted plate area are examined. Each region is approximately (90x90) square microns. These regions are selected from the area immediately under the impact crater to locations not physically affected by the impact.

The polymorphic transformation results from shock- loaded iron have been studied in several publications. Wang, S.J. et al. have studied phase transition in shock- loaded iron [9]. According to Wang, martensitic transformation α (BCC) in iron under shock-loading expressed a reversible and transient nature. He observed the transformation α ε (BCC HCP) in iron under shock- loading. The results indicate two sequential martensitic reversible α-phase transformations in the refined microstructural fingerprints. These transformations occur even if no 'ε' is retained in the post-shock samples. His observation of ambient temperature and atmospheric conditions shows that A36 Steel is stable in its BCC (α)- phase body-centered-cubic (BCC) crystal structure.

A similar behavior could also be observed in 304L steels. At high impacts or pressures, some phase changes occur. According to Wang, BCC takes the form of HCP (ε), in other words, switch to the network (HCP) [8].

While the phase diagram for iron under hydrostatic pressure is well established, it is difficult to ascertain what happens in iron when subjected to shock loading. Understanding dynamic phase evolution is closely related to many iron and steel applications in blast and shock handling conditions, which should agree with Wang [4,9]. The results of microscopic examination of test samples are viewed. Examination of the prepared samples in the study depended on two kinds of microscopy EBSD and XRD. The first one is used to find the unit cell of the crystal system and determine the phase percentage with microstructure maps of the grain and phase. The second one is used to measure the lattice parameters and the orientation.

In crystallography, crystal structure is an arrangement of atoms in a framework pertinent to the type of crystal called a unit cell. A set of atoms is arranged periodically and repeated in three dimensions on a lattice. Crystal lattices have an extended range of regular orders. The distance between a unit cell and one next to it is called Lattice-Distance. The three most common unit cells' arrangements are discussed in the following sections, namely Body-Centered-Cubic (BCC), Face Centered Cubic (FCC), and Hexagonal Close Packed (HCP). These arrangements are referred to as a particular phase structure [8]. Table 1 shows the chemical composition of 304L steel.

HY 100 Steel

High yield HY-100 steel is a unique alloy known for its employment in heavy constructions and has many global applications. The quenched and tempered low carbon alloy has high yield and impact strength (minimum yield strength of 100 ksi). Additionally, It also provides good ductility, first-class toughness, corrosion resistance, and weldability. These properties make HY-100 an ideal candidate for applications in heavy manufacturing, pressure vessels, and petrochemical industries. Traces of Chromium and Nickel in HY-100 give it the desired corrosion resistance properties, which is very well suited in naval construction. To combat the Soviet Akula class's threat, the U.S. Navy responded with the Seawolf class of nuclear attack submarines designed with HY-100 steel alloy hulls to enable deep diving. Since HY-100 is roughly 20 percent stronger than previously used HY-80 steel, submarines can dive up to depths of two thousand feet, with crush depth estimates of 2400-3000 feet [2].

High-velocity impact on metals often causes surface damage and permanent deformation. This effect can only be detected by the Electronic Spectral Microscope (ESM) on the crystalline and atomic levels.

The physical characteristics and molecular structure of HY-100 steel are well known. Backscatter Diffraction and Transition Electron Microscopy have identified evidence of microstructural phase transition and modifications. According to Hixon, Gray, and Dougherty, who discovered that body-centered cubic (BCC) alpha-iron (α) undergoes a fully reversible phase transition to Hexagonal Close Packed (HCP) epsilon-iron (ε) at room temperature and 13.00 GPa[4-6].

Scope

The effects of high-speed velocity impact on the crystalline

structure and material phase changes due to impacts are studied herein experimentally. We examine the high-speed impact on the crystalline structure's inevitable phase change, let alone the atomic reorganization, resulting from the impact on the HY-100 steel in particular. The effects of an impact on the crystalline structure are assessed by impacting HY-100 steel plates (15.4 x 15.4 x1.27 cm) with Lexan projectiles. A two-stage light gas gun accelerates these projectiles to a velocity of 6.70 km/sec at the point of the impact. The impacted plates' surfaces are prepared as required for inspection by the Electron Back Scatter Diffraction (EBSD) microscope. Ten regions on each impacted plate area are examined. Each region is approximately (90x90) square microns. These regions are selected from the area immediately under the impact crater to locations that are not physically affected by the impact.

Background and Definitions

The polymorphic transformation results from shock- loaded iron have been studied in several publications. Wang, S.J. et al. have studied phase transition in shock- loaded iron. According to Wang, martensitic transformation α (BCC) in iron under shock-loading expressed a reversible and transient nature. He observed the transformation α ε (BCC HCP) in iron under shock- loading. The results indicate two sequential martensitic reversible α-phase transformations in the refined microstructural fingerprints. These transformations occur even if there is no 'ε' is retained in the post-shock samples. His observation, at ambient temperature and atmospheric conditions, shows that A36 Steel is stable in its BCC (α)- phase body-centered-cubic (BCC) crystal structure. A similar behavior could also be observed in HY100 steels. At high impacts or pressures, some phase changes occur. According to Wang, BCC takes the form of HCP (ε), in other words, switch to the network (HCP) [8]. While the phase diagram for iron under hydrostatic pressure is well established, it is difficult to ascertain what happens in iron when subjected to shock loading [4]. Understanding dynamic phase evolution is closely related to many iron and steel applications in blast and shock handling conditions, which should agree with Wang [9].

Crystalline Phase

In crystallography, crystal structure is an arrangement of atoms in a framework pertinent to the type of crystal called a unit cell. A set of atoms is arranged periodically repeated in three dimensions on a lattice. Crystal lattices have an extended range of regular order. The distance between a unit cell and one next to it is called Lattice-Distance. The three most common unit cells' arrangements will be discussed in the following sections, namely Body- Centered-Cubic (BCC), Face Centered Cubic (FCC), and Hexagonal Close Packed (HCP). These arrangements are referred to as a particular phase structure [8].

HY-100 Bonding and Structure

Steel is an iron-based alloy that contains carbon, plus small amounts of other elements. Like most metal- alloys, HY-100 Steel crystallizes in one of three very common micros-structures: BCC, FCC, and HCP, o◊a combination between the three. In all three structures, the number of equidistant nearest neighbors (coordination number) is 8 for BCC and 12 for each HCP and FCC. The nearby FCC structure neighbors are at the corners of a cube surrounding the center's metal atom [5]. In the HCP and BCC structures, the atoms pack in layers like stacked cannonballs or billiard balls, with a six-coordinate arrangement. Each atom also has six more adjacent neighbors from layers above and below. Figures 1, 2 show the spatial coordination representation of the three structures. [8]. Table 1 shows the chemical composition of HY-100 steel.

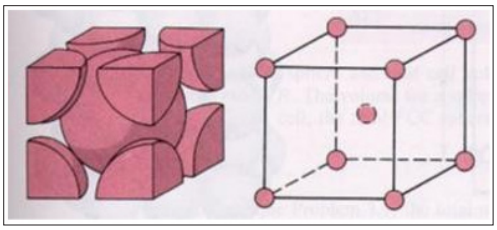

Figure 1: BCC Structure. Atoms are arranged at the corners of the cube, with another at the cube center. The coordination number is 8 [5].

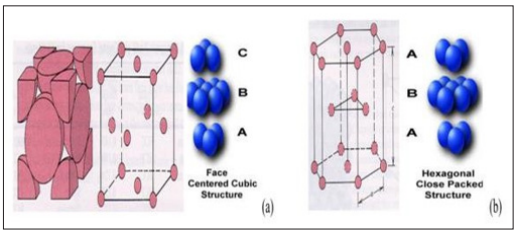

Figure 2: (a) FCC Structure Atoms are arranged at the cube's corners with other atoms at the cube Center. The coordination number is 12. (b) HCP Structure Atoms are positioned at the corners of the cube with other atoms at the cube center. The coordination number is 12 [8].

Table 1: Chemical Composition (%) of HY-100 [1]

Elements	Symbols	HY100
Iron	Fe	92.8 – 96.2
Nickel	Ni	2.25 – 3.50
Chromium	Cr	1.00 – 1.80
Manganese	Mn	0.10 – 0.40
Carbon	C	0.12 – 0.20
Copper	Cu	0.25
Molybdenum	Mo	0.20 – 0.60
Silicon	Si	0.15 – 0.35
Phosphorous	P	0.025
Vanadium	V	0.03
Sulfur	S	0.025
Titanium	Ti	0.02

Twining Concept in Crystals

When a crystal is subjected to different stress or temperature/ pressure conditions than those for which it has initially been formed, two or more intermediate crystals form regularly and cyclically. These symmetric intergrowths of crystals are called twinned crystals. One crystal's points are shared as lattice points with another crystal, adding apparent symmetry to the crystal pairs.

Twinning is essential to recognize because this feature is used for mineral identification. Twinning occurs by cooperative displacement of atoms as exemplified in the (111) direction. The result of twinning is to produce a permanent shape change (plastic deformation) [10]. A twin boundary, or composition surface, separates the two crystals. Atomic dislocation may generate twinning shear. The distance of each atom's position is related to the original system and the twin lattice [11,12].

Background and Definitions

The polymorphic transformation results from shock-loaded iron have been studied in several publications. Wang, S.J. et al have studied phase transition in shock-loaded iron [6]. According to Wang, martensitic transformation α (BCC) in iron under shock-loading expressed a reversible and transient nature. He observed the transformation α ε (BCC HCP) in iron under shock-loading. In the refined microstructural fingerprints, results were indicative of two sequential martensitic transformations in the reversible α phase transition, even though no 'ε' is retained in the post-shock samples. His observation, at ambient temperature and atmospheric conditions, shows that A36 Steel is stable in its BCC (α)-phase body-centered-cubic (BCC) crystal structure.

At high impacts or pressures, some phase changes take place According to literature and our own experiments; BCC takes on the HCP (ε) form, in other words, switching to the hexagonal-closed-packed (HCP) lattice. While the phase diagram of Fe under hydrostatic pressure is well- established, it is much more challenging to ascertain what happens in Fe when it is subjected to shock-loading. Understanding dynamic phase evolution is critically relevant to many applications of iron and steels under explosion and shock processing conditions,", accords to Wang [6]. In our documented experiments, the target material is subject to high pressure and temperature over a short time. The impacting momentum range is at velocities between 3 km/sec and 6 km/sec. The damage zone develops in the target within 5 microseconds. Some steel materials go through a reversible phase change when subject to elevated temperature and high quasi-static pressure. It is unknown whether A-36 steel experiences this phase change during a high-velocity impact.

Crystalline Phase

In crystal structure is an arrangement of atoms in a framework pertinent to the type of crystal called a unit cell, which is a set of atoms arranged periodically repeated in three dimensions on a lattice. Crystal lattices have an extended range of regular order. The distance between a unit cell and one next to it is called Lattice-Distance. The arrangements of the three most common unit cells will be discussed in the following sections, namely BCC, FCC, and HCP. These sections are referred to as a particular phase structure [5].

A36 Bonding and Structure

Steel is an iron-based alloy that contains carbon, plus small amounts of other elements. Like most metal- alloys, A36 Steel crystallizes in one of three very common micros-structures: Body-Centered-Cubic (BCC), Face Centered Cubic, (FCC) Hexagonal Close Packed (HCP), or a combination between the three. In all three structures, the number of equidistant nearest neighbors (coordination number) is 8 for BCC and 12 for each HCP and FCC. The nearest neighbors in the FCC structure are at the corners of a cube surrounding the metal atom in the center. In the HCP and BCC structures, the atoms pack in layers like stacked cannonballs or billiard balls, with a six-coordinate arrangement. Each atom also has six more adjacent neighbors from layers above and below. Figures 1, 2, a and b, shows the graphic coordination representation of the three structures [5]. Table 1 shows the chemical composition of A36 steel.

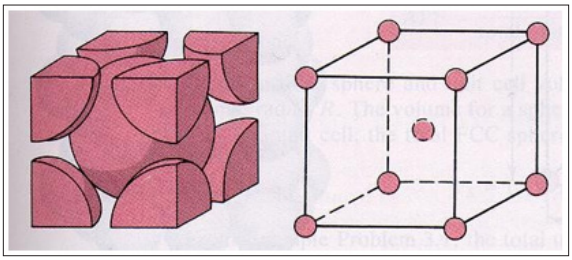

Figure 3: BCC Structure. Atoms are arranged at the corners of the cube with another at the cube center. Coordination number is 8 [5].

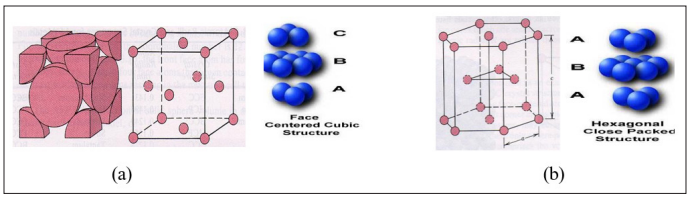

Figure 3: (a) FCC Structure Atoms are arranged at the corners of the cube with other atoms at the cube Center. Coordination number is 12. (b) HCP Structure Atoms are arranged at the corners of the cube with other atoms at the cube center. Coordination number is 12 [5].

Table 2: Chemical Composition (%) of A36 [4]

Element	Symbol	A36 [22]
Iron	Fe	98.0
Nickel	Ni	0.00
Chromium	Cr	0.00
Manganese	Mn	1.03
Carbon	C	0.25 - 0.29
Copper	Cu	0.20
Molybdenum	Mo	0.00
Silicon	Si	0.28
BSD Phosphorous	P	0.04
Vanadium	V	0.00
Sulfur	S	0.05
Titanium	Ti	0.00

Twinning Concept in Crystals

When the crystal is subjected to stress or temperature/pressure conditions different from those under which it originally formed, two or more medial crystals are formed in an orderly, periodic fashion. These symmetric intergrowths of crystals are called twinned crystals. Points of one crystal are shared as lattice points with another crystal, adding apparent symmetry to the crystal pairs. Twinning is considered mysterious phenomena. However, twinning is essential to recognize because this feature is used for mineral identification. Twinning occurs by cooperative displacement of atoms as exemplified in the [111] direction.`

The result of twinning is to produce a permanent shape change (plastic deformation) [7]. Under certain circumstances, crystals, specific conditioning, and re- formation occur, creating the phenomenon that we call twinning. Twinning occurs when two separate crystals share some of the same crystal lattice points symmetrically. The result is a rebirth of two distinct crystals in a variety of configurations. A twin boundary, or composition surface, separates the two crystals. The deformity caused by twinning explained by the twinning surface and direction. Atomic

dislocation may generate twinning shear. Twinning appears as a mirror image on the surface. The distance of each atom's position is related to the original system and the twin lattice [8,9].

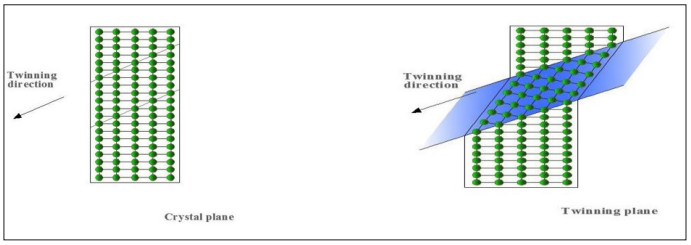

Figure 4: Twinning occurs by cooperative displacement of atoms [8].

Test and Measurement Protocols

The primary source of examination of our specimens is Electron Backscattering Diffraction (EBSD). According to Geochemical Instrumentation and Analysis, EBSD is used to examine and detect the crystalline structure of the A36 steel pre-impact and post- impact. Atomic layers in crystalline materials can diffract the accelerated electrons in the primary beam of a scanning electron microscope (SEM). These diffracted electrons can be detected when they impinge on a phosphor screen and generate visible lines, called Kikuchi bands, or "EBSP's" (electron backscatter patterns). These patterns are effectively projections of the geometry of the lattice planes in the crystal, and they give direct information about the crystalline structure and crystallographic orientation of the grain from which they originate. When used in conjunction with a database that includes crystallographic structure information for phases of interest and with software for processing the EPSP's and indexing the lines, the data can be used to identify the phases based on crystal structure and also to perform fabric analyses on polycrystalline aggregates. In brief, the EBSD device can be useful in many ways [10].

- Analysis technique based on a scanning electron microscope (SEM)
- A measure of the local crystal orientation with a sub-micron spatial resolution
- Use for phase distribution analysis.

Impact Experiment Geometry and Materials

Target plates are mounted to a support plate that is attached to the internal frame of the target chamber.

Figure 4(a) shows the target plate in green and the support plate in red. Figure 7(b) shows the support plate mounted inside the target chamber.

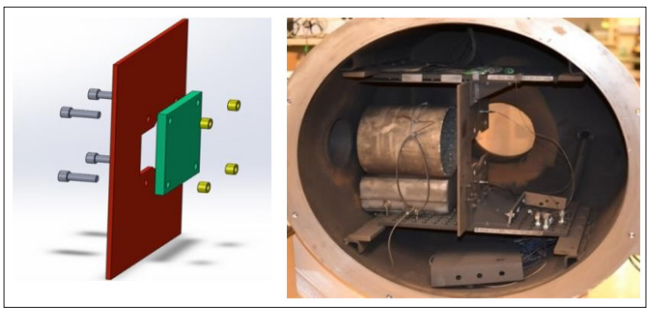

(a) (b)

The target plates are cut into square shapes that fit conveniently inside the target chamber. All target plates have the same dimensions. They are 15.2 cm x 15.2 cm x 1.27 cm. They are impacted with a cylindrical Lexan projectile with a 5.6 mm diameter and 8.6 mm length. An A36 steel target plate and Lexan projectile are shown in Figure 5. The target plates are impacted with projectiles at speeds selected to induce significant plastic deformation without completely penetrating the target. The visually observable damage on the front and back sides of a typical target plate is shown in Figure 6. The crater diameter can be slightly more than three times the projectile diameter (~ 17 mm) for the faster impact velocity. The depth of the crater measured from the flat region on the front surface was up to 6.6 mm and the bulge on the back surface was up to 3.5 mm, measured from the flat region of the back surface [11].

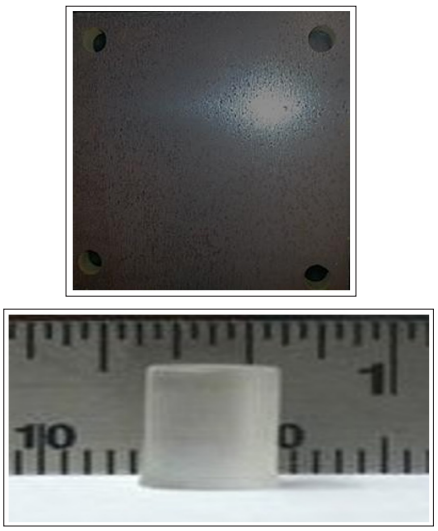

Figure 6: A36 Target plate before impact and Lexan projectile (not shown to the same scale) [13].

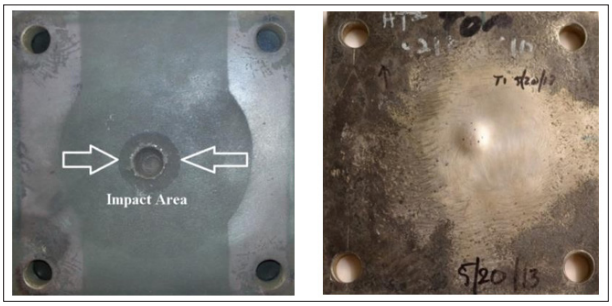

Figure 7: Visible damage on an A36 steel target on the Front sides (Left) and backside (Right).

Target Plate Sectioning and Cross-Section Zones Slicing

Each impacted plate was initially cut in half through the center of the impact crater. The target materials were further cut into a T-Shape so that six different cross-sections could be exposed and prepared for microstructural analysis. All cutting procedures were controlled to minimize the addition of temperature to the cutting surfaces. A water jet machine was used to make the necessary cuts in the steel targets to obtain the T-shaped bar. The water jet process cools while cutting to help eliminate heat-induced changes to the microstructure. Figure 7 shows the results of cutting at various stages, including a target plate being prepared for water jet cutting. A top view of the T-shaped bar is shown in Figure 7, along with the corresponding dimensions.

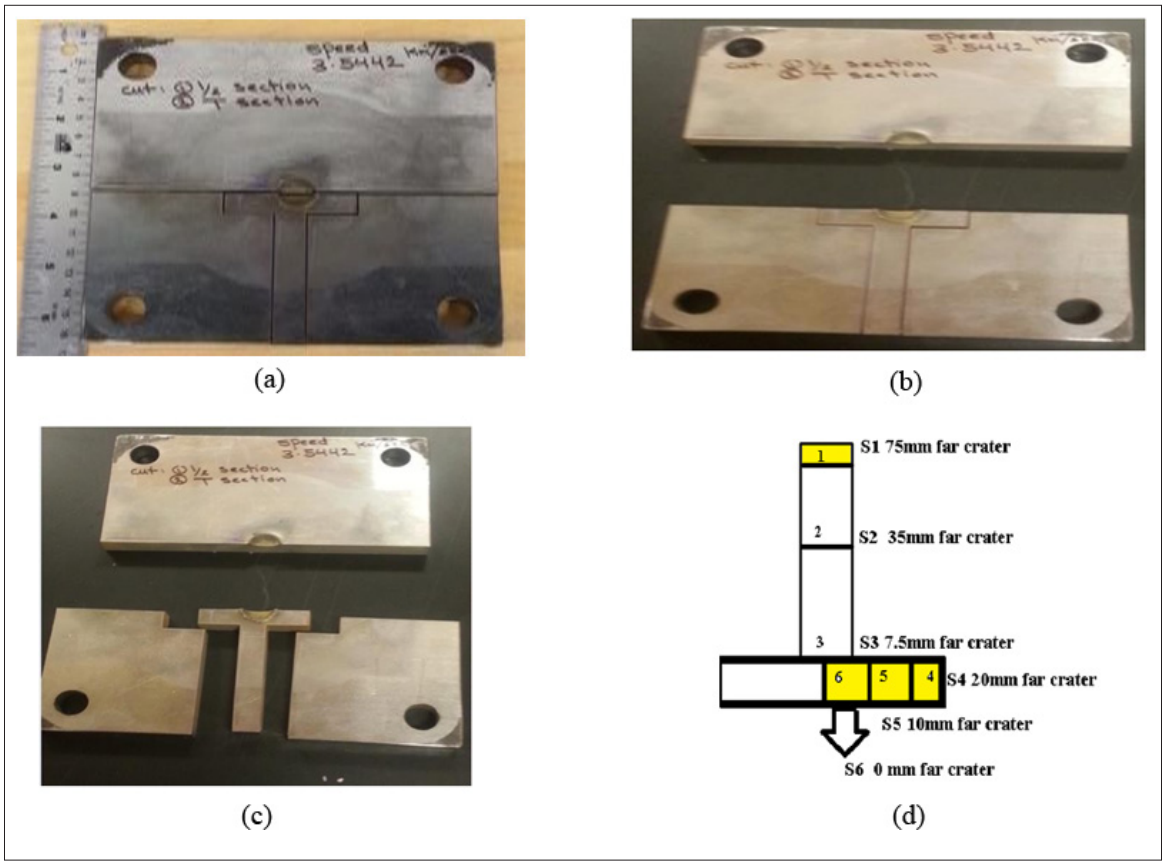

Figure 8: (a) Cut lines on a target plate, (b) Target cut in half, (c) Finished T-section ready for further Dividing and (d) T-shaped bars with dimensions

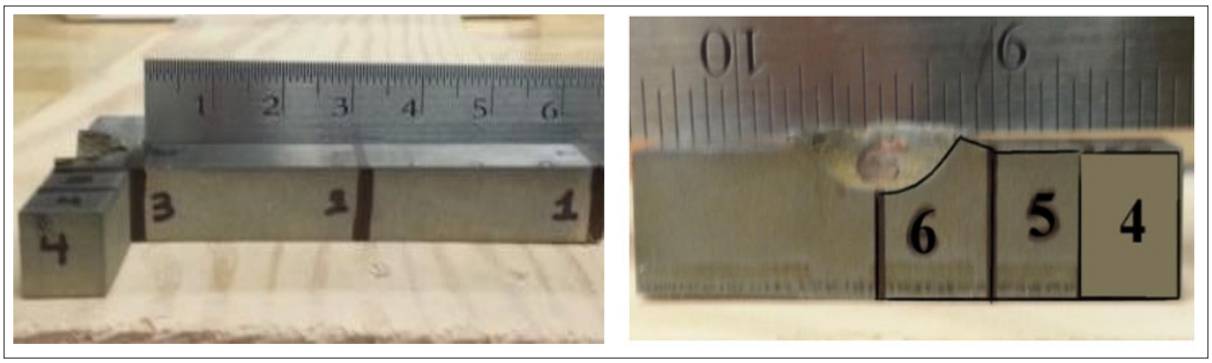

Figure 9: Location of six cross-sectional regions used for microstructural analysis [13].

Selected Locations of the center of the slide for EBSD viewing are designated as follows:
Sample (1): Centered 75 mm away from the impact crater, the thickness is 12.7 mm.
Sample (2): Centered 35 mm away from the impact crater, the thickness is 12.7 mm.
304L steel
Sample (3): Centered 7.5 mm from the impact the thickness is 12.7 mm, the other side of the T- Section.
Sample (4): Centered 20 mm and thickness is 12.7 mm.
Sample (5): Centered 10 mm and thickness is 12.7 mm.
Sample (6): Centered at the impact area
All materials and methods that have been used in the work must be stated clearly. Subtitles should be used when necessary.

Test and Measurement Protocols

The primary source of examination of our specimens is (EBSD). The patterns effectively project the geometry of the lattice planes in the crystal. They give direct information about the crystalline structure and crystallographic orientation of the grain from which they originate.

Table 3: Chemical Composition (%) of 304L [3]

Elements	Symbols	304L
Iron	Fe	66.9 - 74.5
Nickel	Ni	8.00 – 10.5
Chromium	Cr	17.5 – 19.5
Manganese	Mn	0.00 – 2.00
Carbon	C	0.00 – 0.03
Copper	Cu	0.00
Molybdenum	Mo	0.00
Silicon	Si	0.00 – 1.00
Phosphorous	P	0.00 – 0.05
Vanadium	V	0.00
Sulfur	S	0.00 – 0.02
Titanium	Ti	0.00

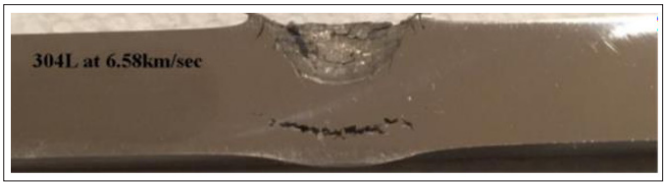

Figure 10: Crater zone in 304L targets subject at 6.58Km/s.

Impact Experiment Geometry and Materials

Figure-3 shows photographs of the 304L target plates before and after impact, along with the sample preparation cutting T-shaped geometry, like the geometry used for the A36 targets. All the Target plates' details are mounted to a support plate explained in our previous work [13-16]. The target plates are cut into square shapes that fit conveniently inside the target chamber. Target plates are mounted to a support plate attached to the internal frame of the target chamber. All target plates have the same dimensions. They are 15.2 cm x 15.2 cm x 1.27 cm. They are impacted with a cylindrical Lexan projectile with a 5.6 mm diameter and 8.6 mm length. The target plates are impacted with projectiles at speeds selected to induce significant plastic deformation without completely penetrating the target. The visually observable damage on a typical target plate's front and back sides is observed. The crater diameter can be slightly more than three times the projectile diameter (~ 17 mm) for the faster impact velocity. The crater's depth measured from the flat region on the front surface was up to 6.6 mm, and the bulge on the back surface was up to 3.5 mm, measured from the flat region of the back surface. The visually observable damage on the front and back sides of a typical target plate is shown in Figure 1. The crater diameter can be slightly more than three times the projectile diameter (~ 17 mm) for this impact velocity.

Target Plate Sectioning and Cross-Section Zones Slicing

Each impacted plate was initially cut in half through the center of the impact crater. The target materials were further cut into a T-Shape to expose six different cross-sections and prepare for microstructural analysis. A water jet machine cutting procedures were controlled to minimize the addition of temperature to the cutting surfaces. Figure -3 shows the selected locations of the center of the slide for EBSD viewing are designated as follows:

Sample (1): Centered 75 mm away from the impact crater, the thickness is 12.7 mm.
Sample (2): Centered 35 mm away from the impact crater, the thickness is 12.7 mm.
Sample (3): centered 7.5 mm from the impact (the thickness is 12.7 mm,) on the other side of the T- Section.
Sample (4): Centered 20 mm and thickness is 12.7 mm.
Sample (5): Centered 10 mm and thickness is 12.7 mm.
Sample (6): Centered at the impact area.

Specific regions are selected and marked with letters (A, B, C, D, etc.) in any of these samples, as shown in Figures (8 and 9). The sample number and the area letter constitute the EBSD inspection and analysis locations.

HY 100 steel

The primary source of examination of our specimens is (EBSD). The patterns effectively project the geometry of the lattice planes in the crystal. They give direct information about the crystalline structure and crystallographic orientation of the grain from which they originate.

Impact Experiment Geometry and Materials

All the Target plates' details are mounted to a support plate explained in our previous work [14,16]. The target plates are impacted with projectiles at speeds selected to induce significant plastic deformation without completely penetrating the target. The visually observable damage on the front and back sides of a typical target plate is shown in Figure 3. The crater diameter can be slightly more than three times the projectile diameter (~ 17 mm) for the faster impact velocity.

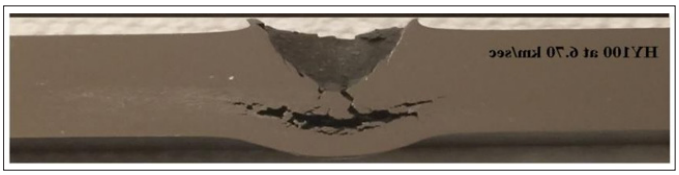

Figure 11: Crater zone in HY100 targets subject at velocities as indicated.

Target Plate Sectioning and Cross-Section Zones Slicing

Each impacted plate was initially cut in half through the center of the impact crater. The target materials were further cut into a T-Shape so that six different cross-sections could be exposed and prepared for microstructural analysis. All cutting procedures were controlled to minimize the addition of temperature to the cutting surfaces. Figure 4 shows the Selected Locations of the center of the slide for EBSD viewing are designated as follows:
Sample (1): Centered 75 mm away from the impact crater, the thickness is 12.7 mm.
Sample (2): Centered 35 mm away from the impact crater, the thickness is 12.7 mm.
Sample (3): centered 7.5 mm from the impact (the thickness is 12.7 mm,) on the other side of the T- Section.
Sample (4): Centered 20 mm and thickness is 12.7 mm.
Sample (5): Centered 10 mm and thickness is 12.7 mm.
Sample (6): Centered at the impact area.

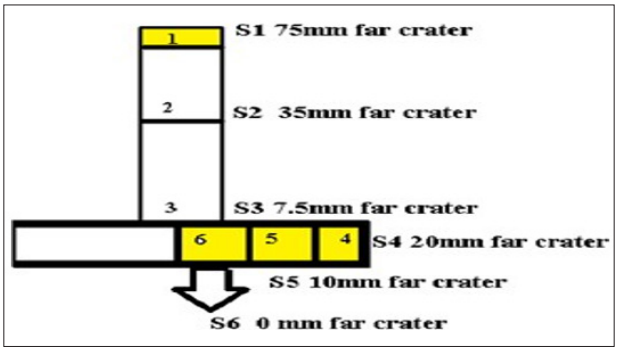

Figure 12: T-shaped bars with dimensions regions used for microstructural analysis.

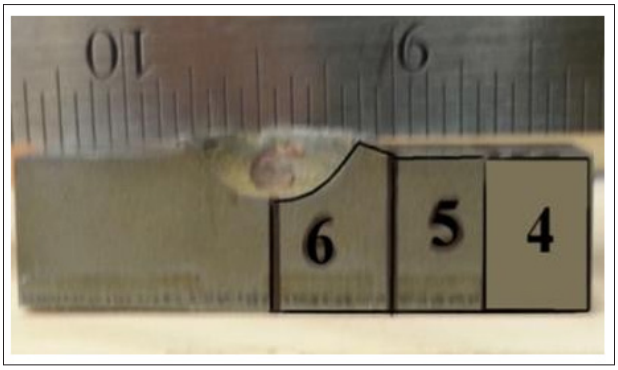

Figure 13: Location of six cross-sectional

Test Results

A36: Phase Ratio

EBSD has been used to examine the impacted samples for the three different suggested impact speeds. Figure 4 a 2-D front view and side view for pre-impact specimen inspection Figure 8 shows a cross-section view of an impacted specimen. The view indicates the crack area and what to consider the near impact region: otherwise, regions are designated as distant spots.

Predetermined locations are selected for EBSD viewings. Examination of the prepared samples in the study depended on two kinds of microscopy: EBSD, which is used to find the unit cell of the crystal system and determine the phase percentage with a microstructure map of the grain and phase, and XRD, which is capable of measuring the distance between the lattice parallel surfaces. This distance is known as the lattice constant (d). This work focused on EBSD results.

Figure 9, obtained from EBSD microscopy and shows the grain structure of A36 steel that has not been impacted. It features four views that explain grain, the 350X magnification, and the original length of the map, phase, and crystal unit cell orientation. Table 1 lists non- impact material phase ratios.

Non- Impact EBSD View

The images shown in Figure 9, obtained from EBSD microscopy, show the grain structure of A36 steel that has not been impacted. Figure 9 indicates three views that explain grain, the 350X magnification, and the original length of the map and phase. Table 2 lists non- impact material phase ratios.

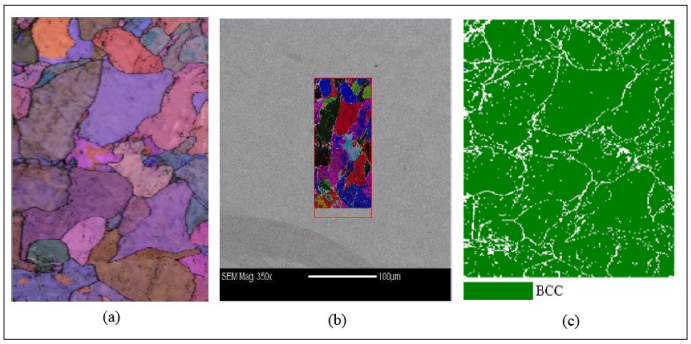

Figure 14: EBSD data from non-impact A36 steel a) grain, b) 350X magnification and the original length of the map, and c) phase map

Table 4: Non-Impact Phase Ratio

Crystal Unit Cell Structures	Non-Impact A36 Steel Phase
BCC	99.98 %
FCC	0.002 %
HCP	0 %

A36 Steel (Impact Velocity of 3.54, 4.51, and 5.80 Km/S)

One A36 target plate from each impact velocity condition was evaluated. The geometry of the damage zone in the A36 target for the three different impact velocities is shown in Figure 10. Depth and width of the crater on the front side is measured with calipers. Enlarged views of the impact section, which is given special attention in scanning for more than one point on the surface of that section, are shown in Figures 10 (a), (b) and (c) for the A36 steel at different impact velocities.

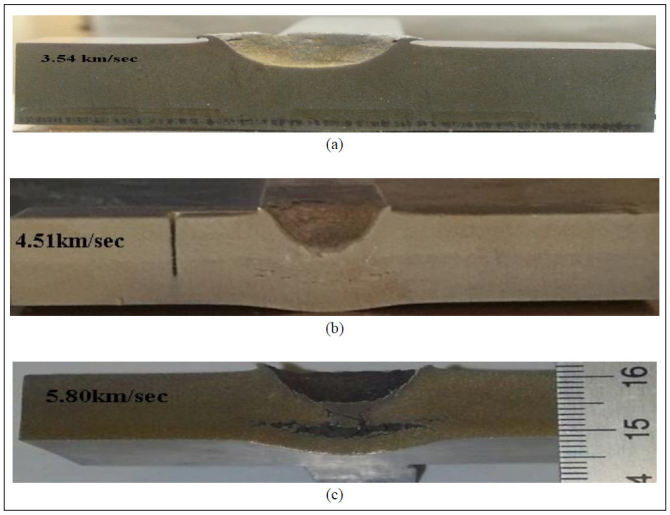

Figure 15: Damage zone in A36 steel targets subject to impact velocities of (a) 3.54 km/s, (b) 4.51 km/s, and (c) 5.80 km/sec [13].

Impact Speed 3.54 Km/S Impact

Figure 11 shows three different slides for EBSD views of the designated location: (a) Centered 75 mm away from impact crater, thickness is 12.7 mm, (b) Centered 35 mm away from impact crater, thickness is 12.7 mm, (c) Centered 7.5 mm from impact, thickness is 12.7 mm from the other side of the T- Section, (d) Centered 20 mm and thickness is 12.7 mm, (e) Centered 10 mm and thickness is 12.7 mm, and (f) Centered at impact area. Notice the apparent twinning traces in the near crater side site. Some minor twinning appears on slide e, and f, and is almost null on slide c. The percentages of crystal modes for an impact speed of

3.54 km/s are tabulated in Table 3.

In the previous section, the tabulated results in Table 3 show the microstructure phase ratios at the reference location. The ratios at the crater center of BCC, FCC, and HCP of A36 steel 90.30 %, 9.5583 %, and 0.1460 %. But at cross-section number 4, the ratios are: 97.076 %, 2.9514 %, and 0.081 %. Clearly, the point nearest the crater shows a higher HCP than that furthest from the crater. The same result is indicated for number 5, in Table 3. Points that seemed to change the most are those in the crater area. Many points were taken, but the points selected in the table "Limited Location" show the many that are scanned by EBSD selected for the study. Depending on the level of confidence, EBSD mapping has shown grain size in the vicinity of the crater, especially on the arc shock limits.

In Table 3, cross-section sample 3, which is located 7.5 mm away from the impact section, one can observe the higher percentage of FCC is significantly increased, as well as a significant reduction of BCC. This significant change can be interpreted as a corresponding transformation of phases between the BCC 96.35 % and FCC 3.629%. Additionally, a new phase started to appear. Thie phase is the HCP 0.079 %. However, the most significant change of the BCC was visible precisely at the impact area that is shown at sample 6, location C. At that section, on, BCC was 90.30 %, FCC 9.56 %, and HCP 0.15%.

Table 4 lists results for A36 steel alloy tests at 4.51 km/s impact. At this speed, a crater has begun to appear. The pattern observed in Table 4 did not modify as expected for BCC to decrease further at the same point of the impact section. This situation can be explained by the existence of a crater. The produced crater has absorbed some of the transformation energy due to the resulted strains. Even that has propagated, not only at this section but rather at all sections. However, the HCP did consistently increase proportionally with the increase of speed and the twinning percentage increase.

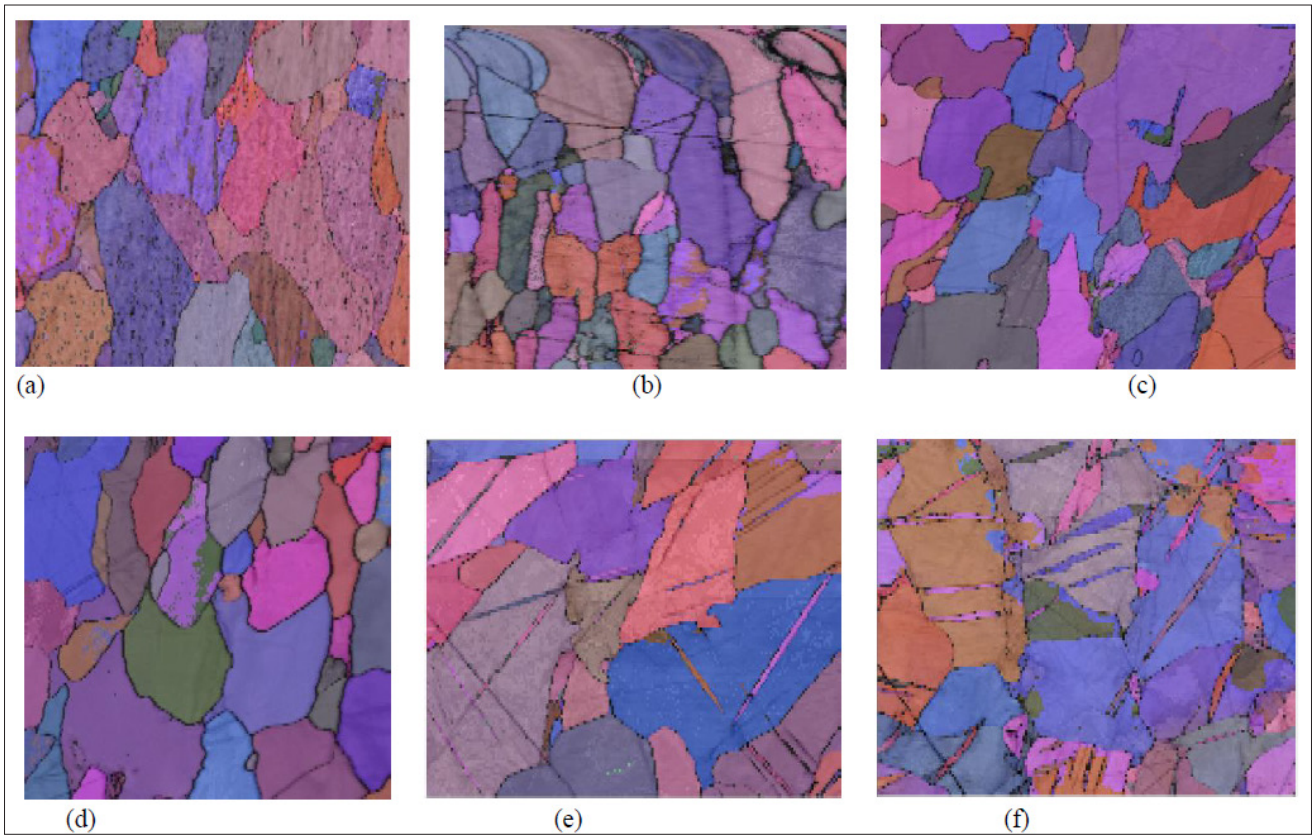

Figure 16: Sample for impacted A36 steel at 3.54 km/sec all cross-sections

Table 5: Location and Dimensions of Cross-Sections for Microstructural Analysis

Section Sample Numbers	Crystal Unit Cell Structures	Phase Content (%)
Sample 1	BCC	98.074
	FCC	1.8366
	HCP	0.063
Sample 2	BCC	98.382
	FCC	1.546
	HCP	0.072
Sample 3	BCC	96.35
	FCC	3.629
	HCP	0.079
Sample 4	BCC	97.076
	FCC	2.9514
	HCP	0.081
Sample 5	BCC	98.1262
	FCC	1.9212
	HCP	0.091
Sample 6 Location C	BCC	90.30
	FCC	9.5583
	HCP	0.1460
Non-Impact A36 Steel	BCC	99.98
	FCC	0.002
	HCP	0

Figure 16 is a qualitative figure that shows the trend of the twinning change.
The most intense twinning region is around the shock center. Quantitatively, Table 3 indicates the ratios of the phase mix relationship. Table 3 shows the estimation of BCC being the dominant phase pre- impact, remaining so after impact in all slides. However, HCP began appearing near impact and existed in the farthest locations, but with insignificant proportion. FCC existed insignificantly pre-impact and became significant post-impact at the impact point andsurrounding area. However, this occurred with a lower percentage and became insignificant again away from the point of impact.

Figure 11 is a qualitative figure showing the trend of twinning change.
The most intense twinning region is around the shock center. Quantitatively, Table 3 indicates the ratios of the phase mix relationship and shows the estimation of BCC being the dominant phase pre- impact, remaining so after impact in all slides. However, HCP began appearing near impact and existed in the farthest locations but with insignificant proportion. FCC existed with insignificance pre-impact and became significant post-impact at the point of impact and the surrounding area. However, this occurred with a lower percentage and became insignificant again away from the point of impact.

Impact Speed 4. 509 km/s Impact
Figure 17 is a qualitative figure showing the trend of twinning change. The most intense twinning region is around the shock center. Quantitatively, Table 4 indicates the ratios of the phase mix relationship and shows an estimation of BCC being the dominant phase pre-impact, remaining so after impact in all slides.

However, HCP began appearing near impact and existed in the farthest locations but with insignificant proportion. FCC existed with insignificance pre-impact and became significant post-impact at the point of impact and the surrounding area. However, this occurred with a lower percentage and became insignificant again away from the point of impact. All parts of Figures 12 of 4.51 km/sec speed show the trend of twinning change starting with sample number 4. The densest twinning region is around the shock center. Quantitatively, all tales of each sample indicate the ratios of the phase mix relationship and show the estimation of BCC being the dominant phase pre- impact, remaining so post-impact in all slides. However, HCP began appearing near the point of impact and existed in the farthest locations but with insignificant proportions. FCC existed with insignificance pre-impact and became significant post-impact at the point of impact and surrounding areas. However, this occurred with a lower percentage and became insignificant again away from the point of impact.

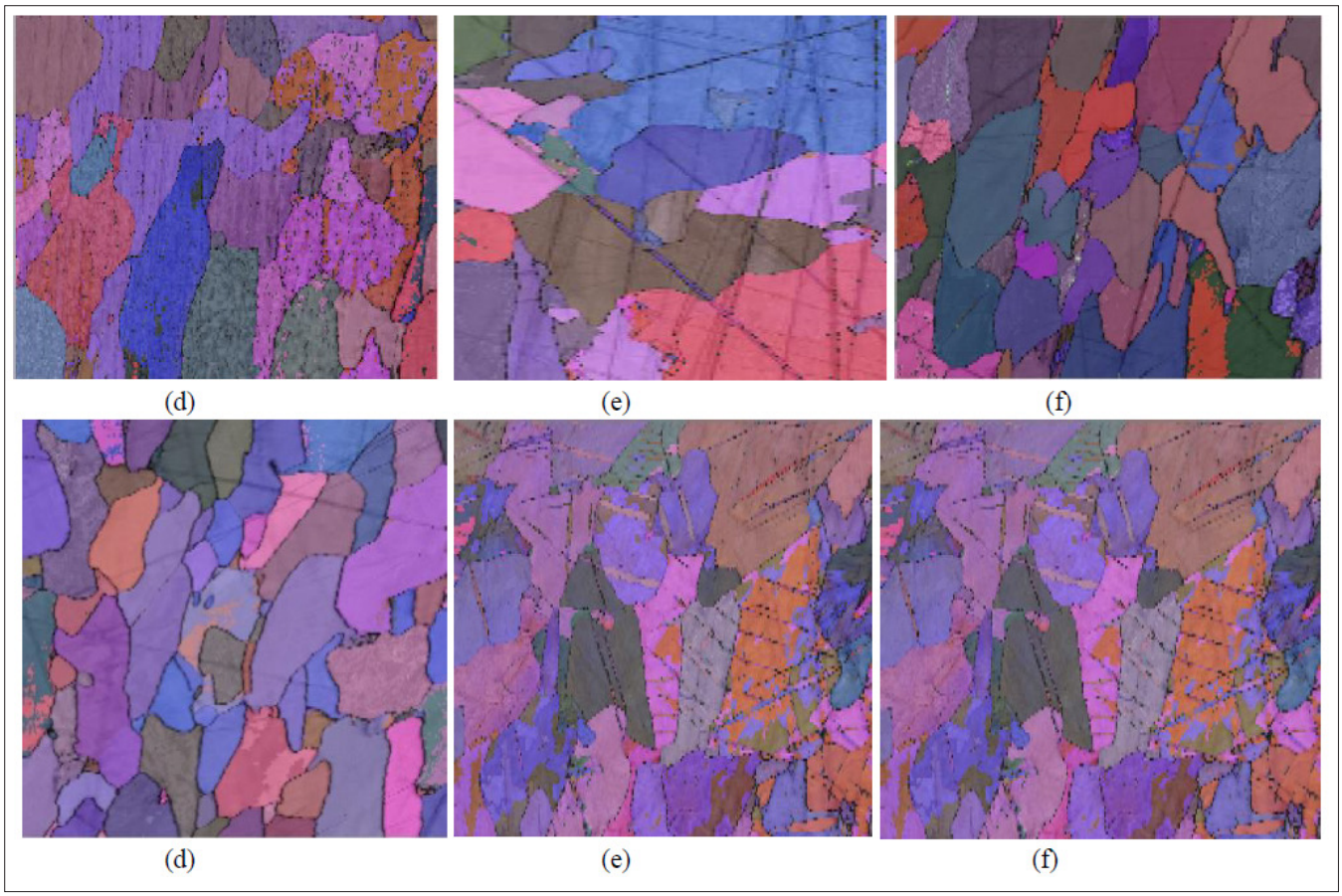

Figure 17: Sample for impacted A36 steel at 4.51 km/sec all Cross-Sections

Table 6: Phase Ratios Changes of A36 Steel at 4.51 km/sec Impact Speed

Section Sample Numbers	Crystal Unit Cell Structures	Phase Content (%)
Sample 1	BCC	98.3105
	FCC	1.6865
	HCP	0.075
Sample 2	BCC	98.507
	FCC	1.485
	HCP	0.078
Sample 3	BCC	96.82
	FCC	3.246
	HCP	0.082
Sample 4	BCC	96.096
	FCC	3.953
	HCP	0.1190
Sample 5	BCC	91.65
	FCC	8.31
	HCP	0.220
Sample 6 Location A	BCC	96.68
	FCC	2.87
	HCP	0.44
Non-Impact A36 Steel	BCC	99.98
	FCC	0.002
	HCP	0

Impact Speed 5.80 km/s Impact

Figure 13 shows three different slides for EBSD views of the designated value. Notice the obvious twining traces in the region near the crater site. Some minor twinning appears on slide d and is almost null on slide e. The percentages of crystal modes for an impact speed of 5.80 Km/s are tabulated in Table 5. Figure 13is a qualitative figure showing the trend of twinning change the most intense twinning region is around the shock center. Quantitatively, Table 5 indicates the ratios of the phase mix relationship and shows an estimation of BCC being the dominant phase pre-impact, remaining so after impact in all slides. However, HCP started to appear near the point of impact and existed in the remote locations but with insignificant proportion. FCC existed with insignificance pre-impact and became significant post-impact at the point of impact and the surrounding areas. However, this occurred with a lower percentage and became insignificant again away from the point of impact. The observation of the samples from the EBSD imaging (post-impact) was that the grain size significantly decreased closer to the impact area (Arc of the projectile) plane that EBSD cannot scan. The error of this area was so high and confidence so little, as shown at location A, so the result is the average of this area. Figure 14 shows samples of (a) non-impact A36 Steel and (b) impact A36 Steel at 5.80 km/sec.

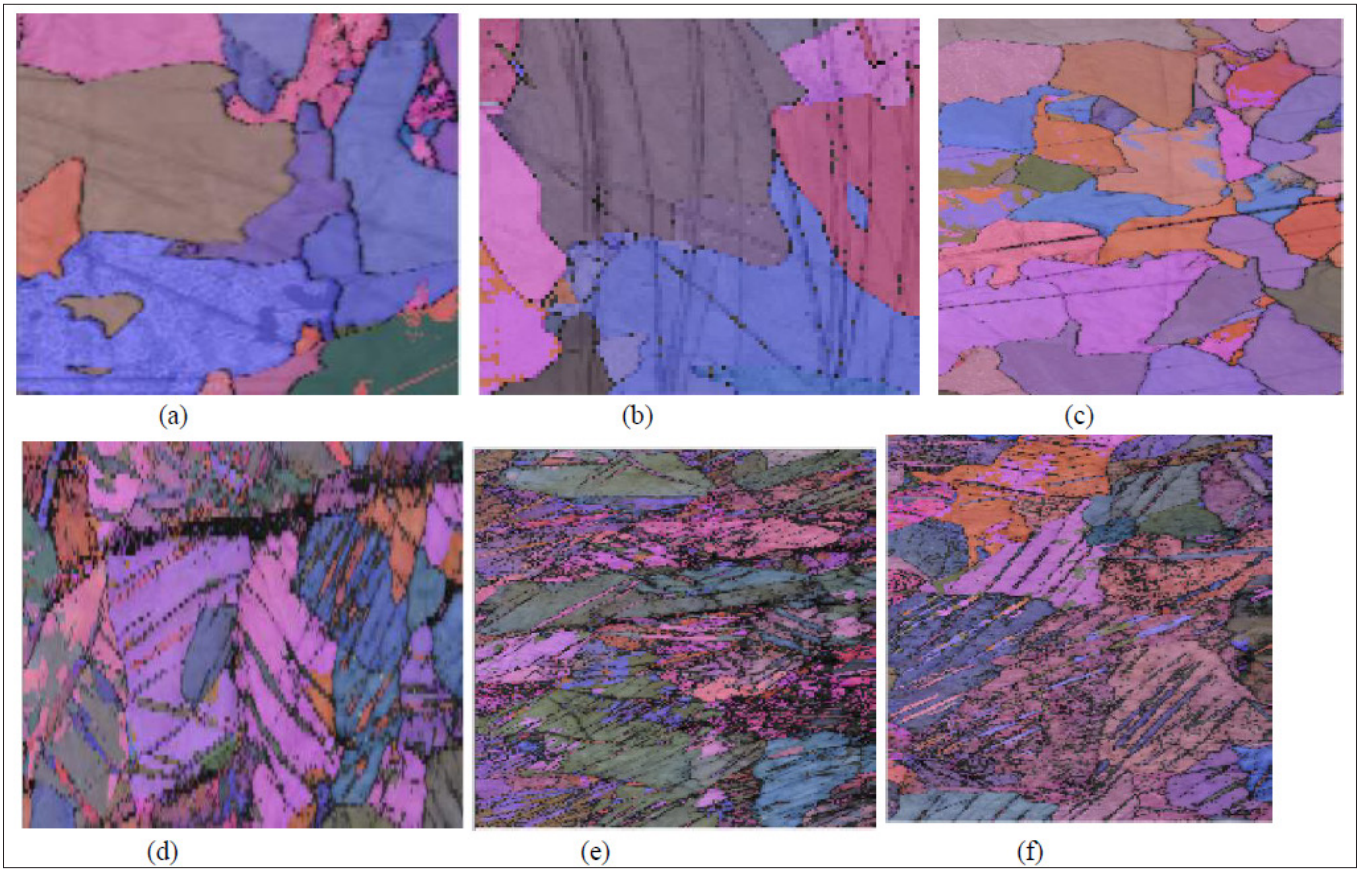

Figure 18: Sample for impacted A36 steel at 5.80 km/sec all cross-sections

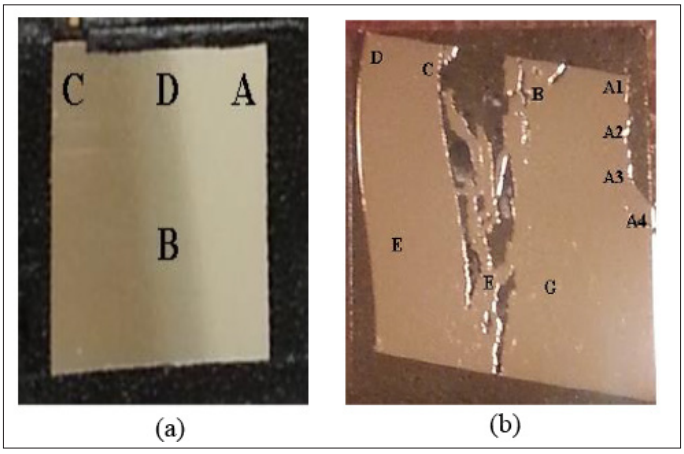

Figure 19: Samples of (a) non-impact A36 steel and (b) impact A36 steel at 5.80 km/sec

Table 7:The Ratio of All Phases Depending on Crater Location A36 Steel at 5.80 km/sec

Section Sample Numbers	Crystal Unit Cell Structures	Phase Content (%)
Sample 1	BCC	98.876
	FCC	10.079
	HCP	0.442
Sample 2	BCC	99.4806
	FCC	0.928
	HCP	0.452
Sample 3	BCC	91.1078

	FCC	9.3748
	HCP	0.523
Sample 4	BCC	98.4246
	FCC	1.6866
	HCP	0.556
Sample 5	BCC	99.03
	FCC	0.88
	HCP	0.88
Sample 6 Location G	BCC	96.180
	FCC	0.6157
	HCP	3.204
Non-Impact A36 Steel	BCC	99.98
	FCC	0.002
	HCP	0

Figure 13 is a qualitative figure that shows the trend of twinning change. The tensest twinning region is around the shock center. Quantitatively, Table 5 indicates the ratios of the phase mix relationship and shows an estimation of BCC, being the dominant phase pre-impact, remains so after impact at all slides.

However, HCP started to appear near impact and existed in the distant location's bus with an insignificant proportion. FCC existed with insignificant pre-impact and became significant after impact at the impact and the neighborhood near impact, however with a lower percentage and became insignificant again for impact.

From the above figures and diagram, it is evident that:
- The non-impacted zone does not have any HCP or a significant amount of FCC
- Increasing impact momentum increased the HCP Percentage.
- Near the crater, the HCP is higher percentile than in a region farther away.

The following points offer some explanation of the observed results: Grain size near impact is compacted near the impact site. The light gas gun uses a powder breech to fire a plastic piston into a pump tube filled with helium or hydrogen. The light gas is compressed as the piston moves through the pump tube. A petal valve separates the light gas from the launch tube, which is under high pressure. Deformation, which consists of slipping and twinning, is highly inelastic at this point; it has become dominant and irreversible.

While examining A36 steel-post impact, not only were the effects visible to the naked eye, but the microstructure was also significantly changed. The post- impact samples were observed under the EBSD microscope to examine the microscopic changes. One observation was the presence of 'twinning.' Twinning was present closer to the impact area and gradually dissipated away further from the impact zone. More twinning was present in the higher speed impact samples than the lower speed impact samples. Twinning was most significant during the testing of the samples from the 5.80 km per second speed impact.

Another observation of the samples from the EBSD imaging (post-impact) was that the grain size significantly decreased closer to the impact area. Further away from the impact area, the grain size was less affected and resembled pre-impact sizes. It was also discovered that the higher speed impact samples showed more evidence of a reduction in grain size than in the slower speed impact samples.

More research is needed to examine different orientations to observe how twinning is formed concerning the impact area. Observing different orientations will also provide further insight into the decreasing grain size around the immediate impact area. Another point of interest would be to test hardness, pre- and post-impact, to examine the behavior change of the material. The presence of HCP (post-impact) leads to the probable conclusion of an increase in brittleness. The preliminary results and observations of post-impact beyond 13 GPa, sub-structural evolution and mechanical behavior of A36 steel agrees with many researches on similar experimental after-shock data on similar iron and alloys, such as in Gray, Hayes, and Hixon [1].

Orientation and Rotation

As in the case of phase-ratio changes, additional evidence of twinning in the examined samples by the EBSD have been tabulated in the section indicated by the evidence of crystalline rotation and orientation. When the changes in the misorientation profile range from [55: 66] degrees in a range of .02 mm length between two points, this is clear evidence of the existence of twinning.

Non-Impact A36 Steel

Misorientation is calculated from the product (or composition) of one orientation and the inverse of the other. This photo shows the angle phase crystalline. Conversely, a change of the order of [0.1: 3.0] degrees indicate no twinning deformation. The following locations and speeds have been examined and plotted to prove further the existence of twinning and degree of plastic deformation related to the relative position compared to the crater area in the three tested impact speeds.

Transition in the grain boundaries of non-impact A36 steel, where the raw material is stable and clear, and the prominent grain of the misorientation angle is in small crystals ranging from 0-1.60° Misorientation measurement for A36 steel target at an impact velocity of 3.54 km/sec at sample location 6 results are shown in Figure15. Each line indicates that the angle is between 55-60° and the percentage of HCP is increased at the crater location at the impact for 3.54 km/sec impact speed.

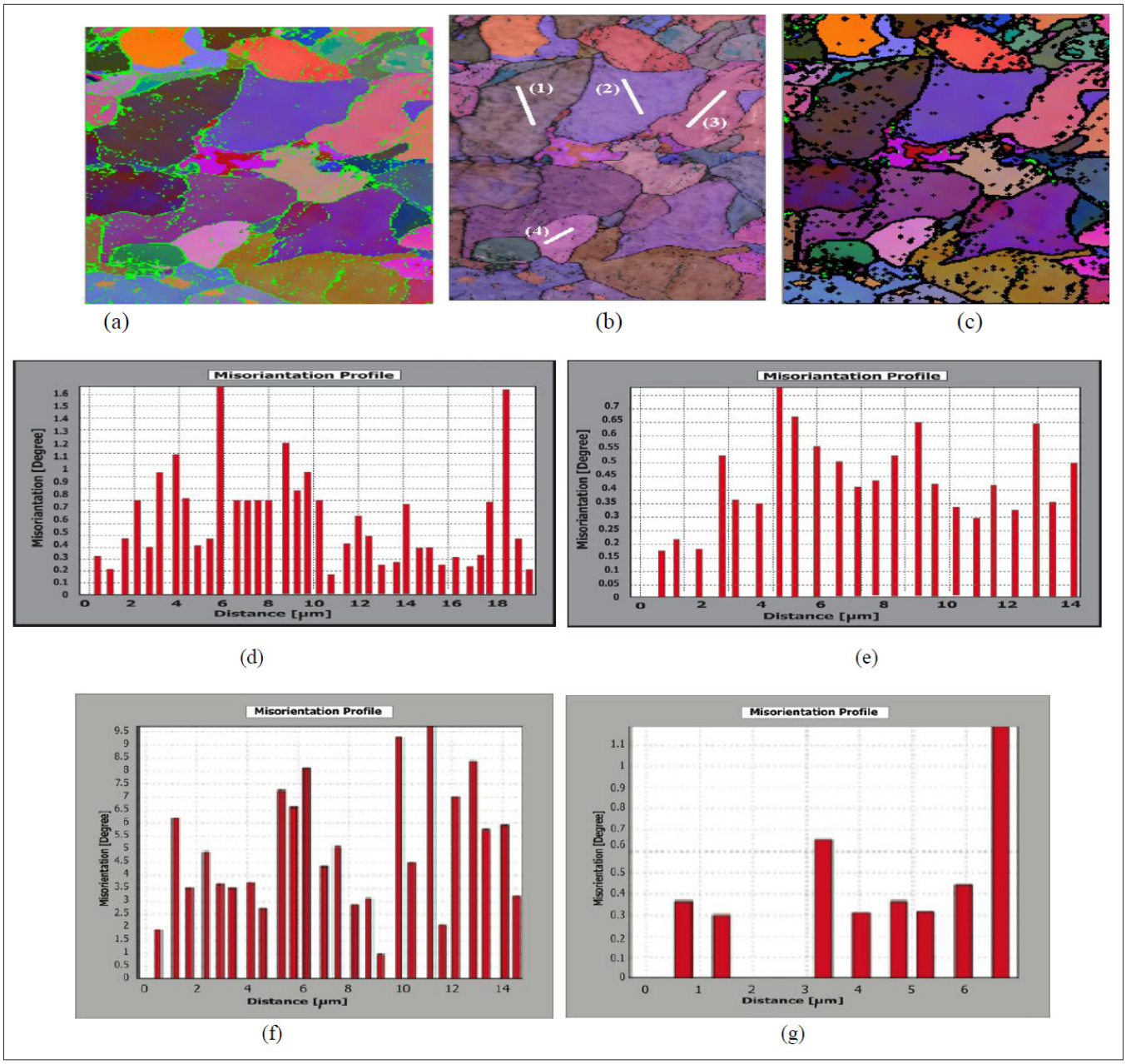

Figure 20: Misorientation angle measured along four different lines in the non-impacted A36 steel: a) EBSD shows less noise, b) EBSD shows grains, c) EBSD shows boundary grains d) Line 1, e) Line 2, f) Line 3, and g) line 4.

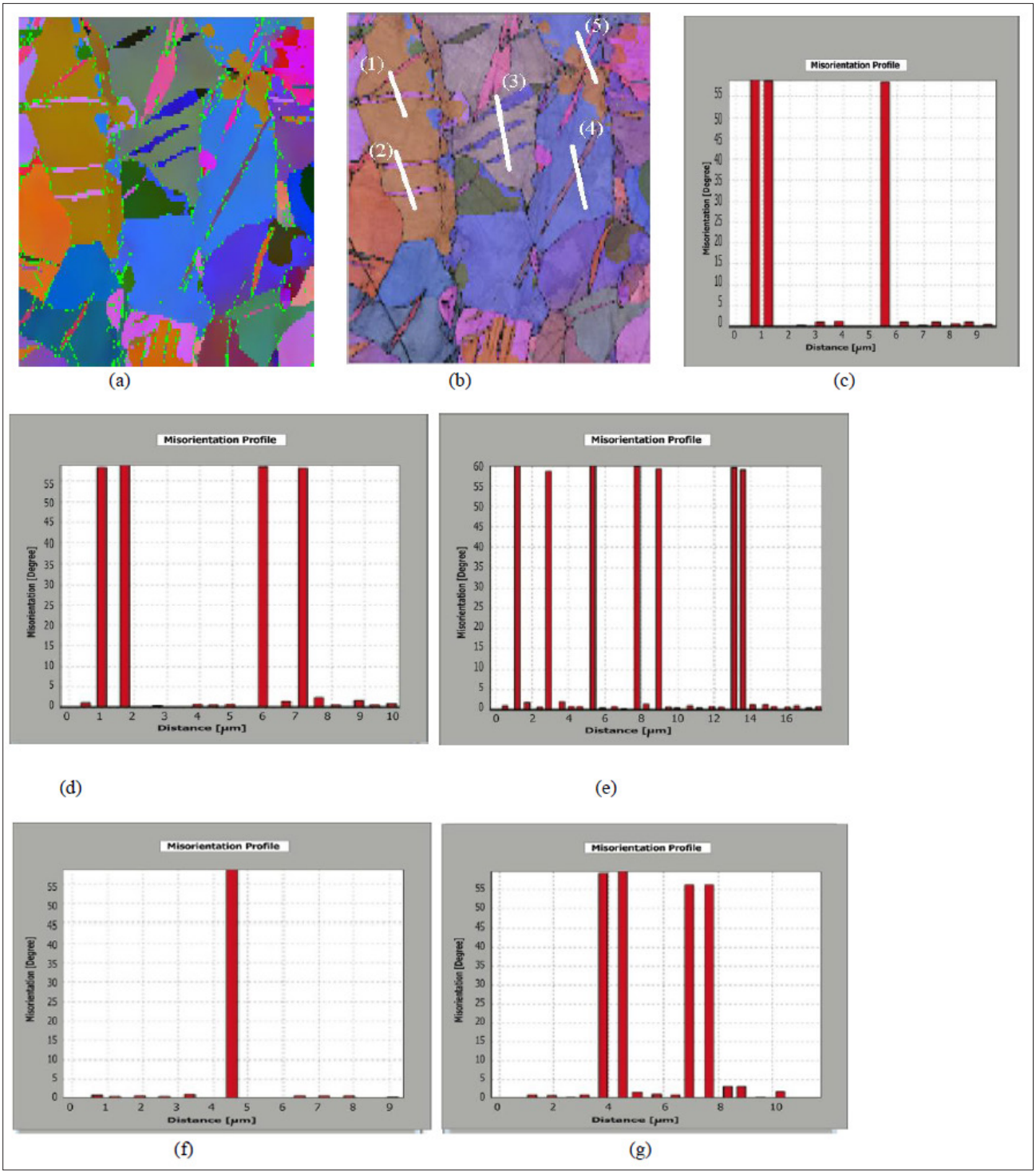

Figure 21: Misorientation angle measured along four different lines in the Impacted A36 steel, sample location 6-A, after impact velocity of 3.54 km/sec: a) less Noise, EBSD b) unenhanced grains; c) Line 1, d) Line 2, e) Line 3, f) Line 4 and G) line 5.

An impact crater at 4.51 km/sec misorientation measurement for A36 steel target with an impact velocity of 4.51 km/sec at sample location 6. Figure 16 shows the plastic deformation on A36 steel at 4.51 km/sec, and all lines that show the angle of this transformation is between (55-60°). The HCP phase was increased in this location, as well as twinning.

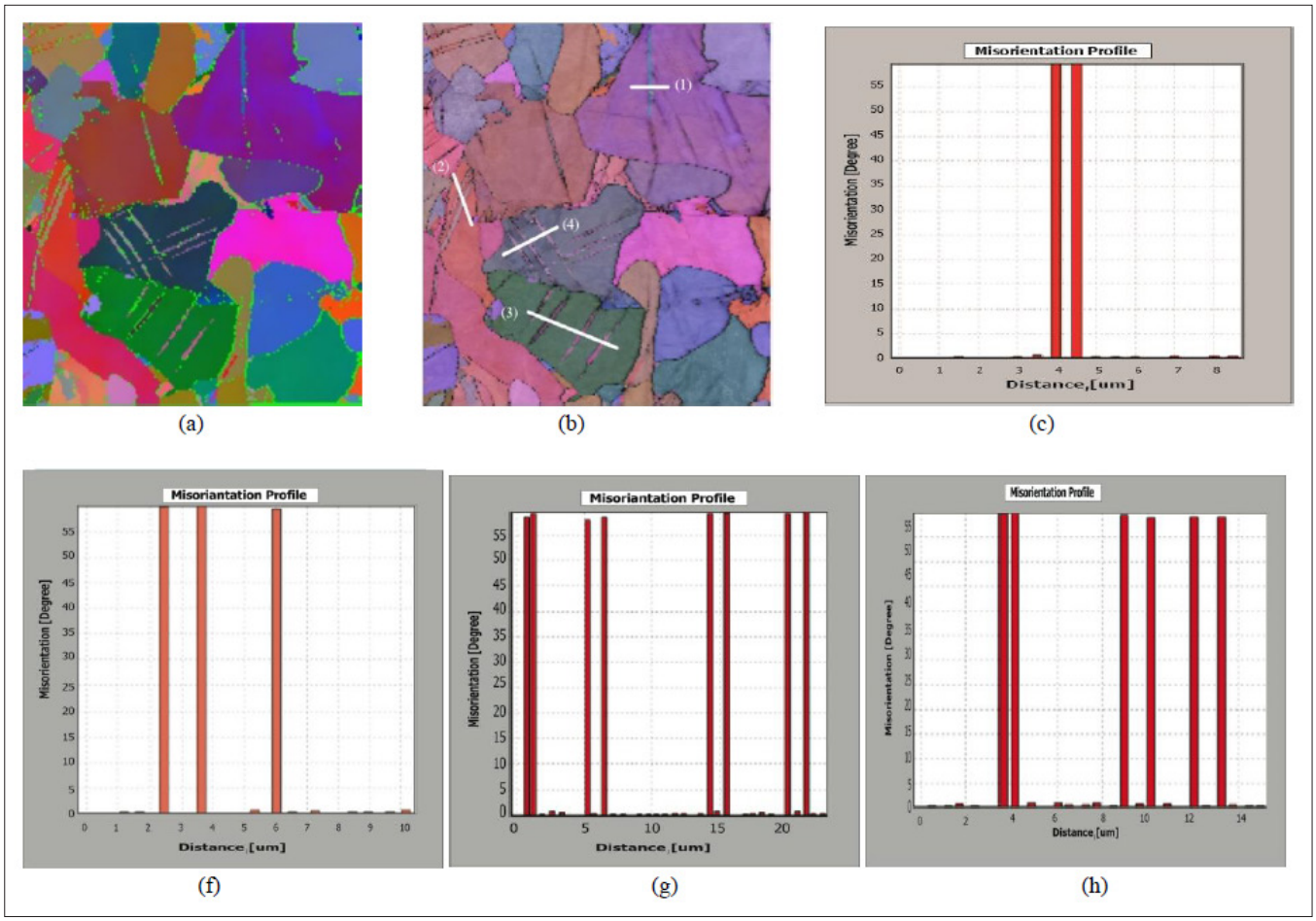

Figure 22: Misorientation angle measured along four different lines in the impact A36 steel, sample location 6-A, after impact velocity of 4.51 km/sec: a) EBSD shows less noise, b) EBSD shows grains; c) Line 1, d) Line 2, e) Line 3, and f) Line 4.

Figure 17: The EBSD microscopy photos show the misorientation angles at 3mm, far from the impact arc of the projectile. The HCP phase in this location increased. Twinning was also noted to have risen- all lines show that the new deformation starts here and changes the phase from BCC to FCC and HCP.

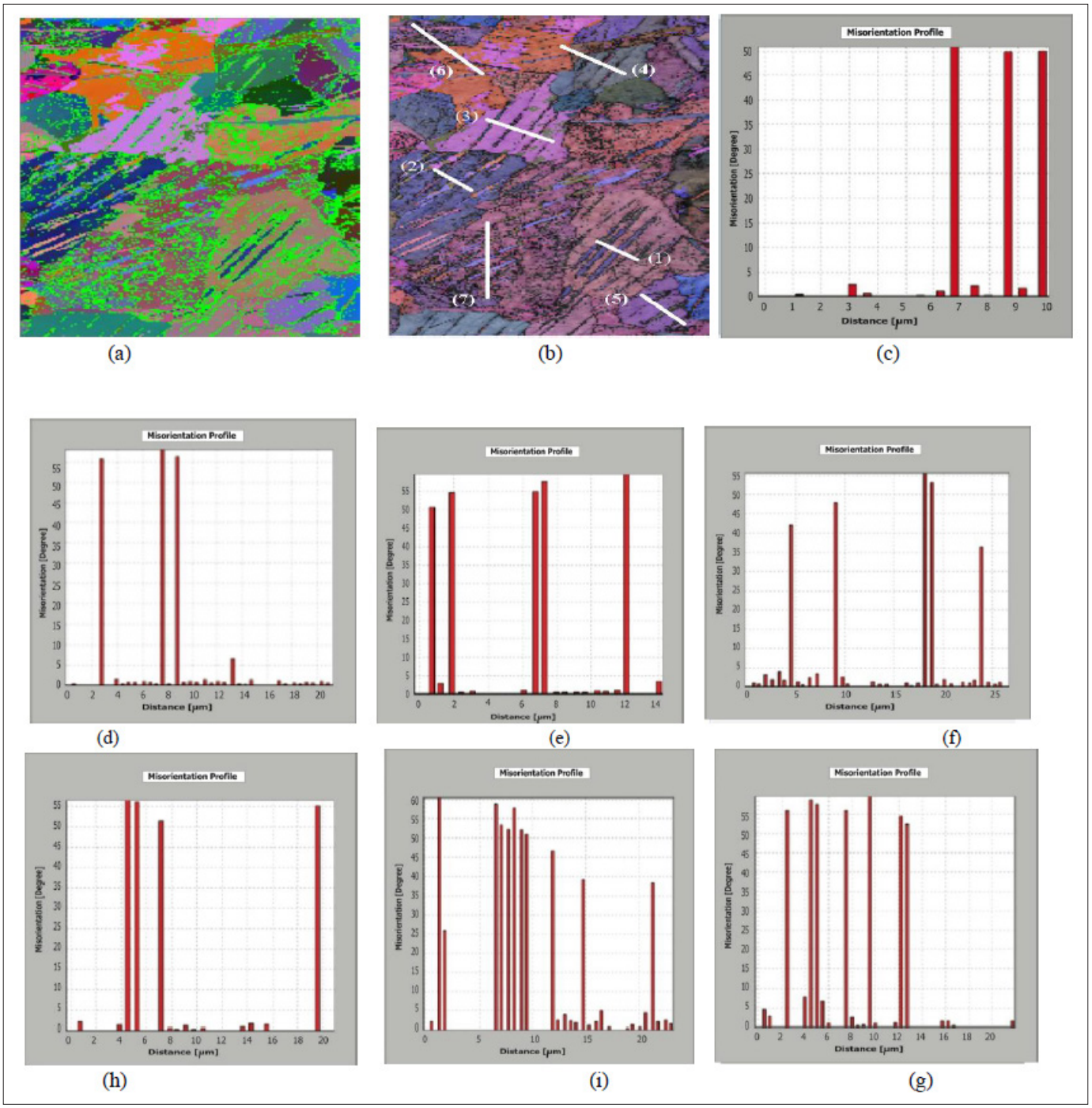

Figurer 23: Misorientation for A36 steel at 5.80 km/sec impact. Sample location 6-G. Misorientation angle measured along four different lines in impact A36 steel, sample location 6-G, after impact velocity 5.80 km/sec: a) EBSD shows less noise, b) shows grains; c, d, e, f, g, h, and i) are lines 1, 2, 3, 4, 5, 6, and 7 respectively.

Results and Discussion

This study of A36 steel microstructure phase change due to high speed beyond 13GPa impact was examined. The changes in body-centered cubic (BCC) and hexagonal close-packed (HCP) phases. An EBSD microscope has been used to detect the changes in several locations with different distances, ranging from a few millimeters to as far as 75 mm from the impact crater. X- ray viewing of such places by EBSD revealed that: a) Significant post-impact changes vary in intensity near and far from the impact, which was intuitively was projected.

b) the tendency of those phase changes is evident to be transient, as suggested by repeated examination of the same spots at different time intervals. The evidence suggests unstable, transitional phase changes. This conclusion is in agreement with previously investigated high purity Fe by Hixon and Gray III, Dougherty, et al., and others [1,12]. c) Twinning appeared near impact area around 1000and 1500 micrometers, and d) at a range closer than 500 micrometers, the EBSD microscope was not able to detect any phase combination.

Table 8: Peak impact pressure in A36 steel targets predicted from simulations [11]

Impact Velocity (km/s)	Location (mm)	Peak Pressure GPa
3.54	a (Crater)	60
3.54	b (20mm)	14.2
4.51	a (Crater)	75
4.51	b (20mm)	14.9
5.80	a (Crater)	93
5.80	b (20mm)	14.9

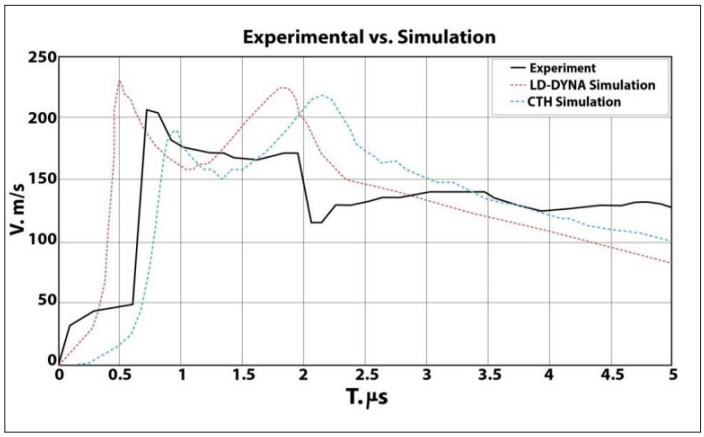

Figure 24: Experimental data and computational simulations of back face velocity versus time during the impact of a Lexan projectile (5.3 km/s) into an A36 steel plate [14].

Table 6: Expresses the location for the selected scanning position relative to the impacted surface and the edges of the plate. This location further indicates the final dimension of the specimens that are prepared for scanning.

Table 9: Location and dimensions of cross-sections for microstructural analysis [11]

Cross- Section Zone	Branch of T-Bar	Planar Distance from Impact Center (mm)	Left Edge Distance from Impact Center (mm)	Dimensions of Cross-Section (mm x mm)
1	Web	75	0	12.7x 12.7
2	Web	35	0	12.7 x 12.7
3	Web	7.5	0	12.7 x 12.7
4	Flange	0	20	12.7x 12.7
5	Flange	0	10	12.7 x 12.7
6	Flange	0	0	12.7 x 12.7 (upper left corner missing)

As for Pressure Time Distribution in Target Plates, the internal pressure in the target plates during impact varies with time and position relative to impact. It was not possible to measure this pressure during experiments [13]. Performed LS- Dyna computational simulations of the trials and predicted the pressure versus time at several points within the target for specific impact velocities. The pressure directly under the impacting projectile is much higher than the pressure far away from the impact point [15,16].

304l Steel

EBSD has been used to examine the impacted samples in one suggested impact speed. Figure 1 shows a cross-section view of an impacted specimen. The picture indicates the crack area and what to consider the immediate impact region: otherwise, regions are designated as distant spots. Examination of the prepared samples in the study depended on two kinds of microscopy: First, EBSD is used to find the crystal system unit cell and determine the phase percentage with a microstructure map of the grain and phase. Second, XRD can measure the distance between the lattice parallel surfaces. This distance is defined as the lattice constant (d) [3].

Non-Impact EBSD Grain Structure View

As Received 304L Steel (non-impact), the results show it has three phases BCC, FCC, and some small percentage of HCP, as shown in figure 4. The actual phase of this kind of steel is BCC and FCC. EBSD effectuates grain Structure Phase Measurements. Figure-5 shows the grains boundary and the magnification of the microscopy 400X and the crystal orientation, with the phase percentage shown in Table-1. EBSD results of 304L steel plate show two phases, BCC and FCC, co- exist in their microstructure, both in significant amounts, yet with a trace of HCP with the non-impact ratios of 33.109 %, 66.718 %, and 0.1724 %. This result shows that the main phase contents of this kind of steel are BCC and FCC. Transition and change locations of the grains inside the crystal of non-impact 304L are examined. Before the shock, the angle range was (0- 1.30°). Because the crystal system and stable raw material were not exposed to any load,304L steel is a heat-resisting metal.

Figure -5 shows the state system, and the misorientation angles are between (45-55°). This state means no orientation or dislocation in the plan of the crystal.

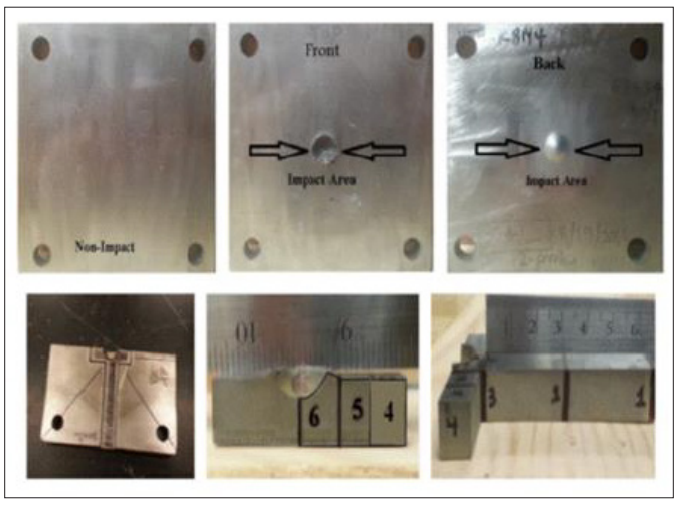

Figure 25: Non-impacts and Impact 30L steel and Impact at 6.58 km/sec. Location of six cross-sectional regions used for microstructural analysis

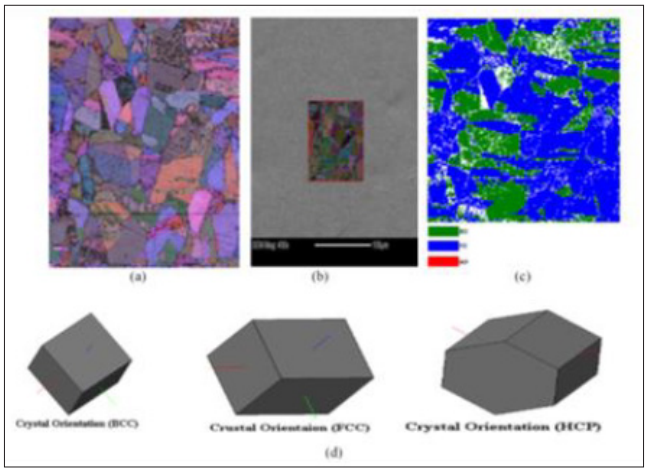

Figure 26: 304L Non–Impact microstructure photo of EBSD

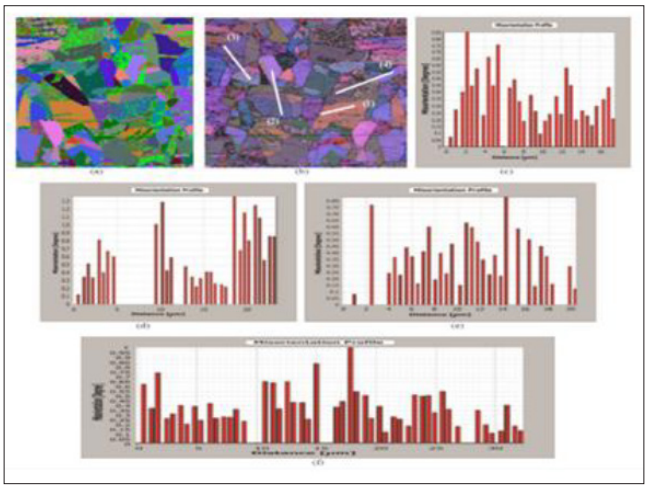

Figure 27: Misorientation angle measured along four different lines in the non-impacted 304L steel, the sample shows: a) EBSD shows less noise, b) EBSD shows grains, c) Line 1, d) Line 2, e) Line 3, and f) Line 4.

Table 10: Non-Impact Phase Percentages of 304L Steel

Crystal Unit Cell Structures	Non-impact 304L Steel Phase %
BCC	33.1092
FCC	66.718
HCP	0.1724

Impact Velocity of 6.7 Km/s on 304l Steel

One 304L target plate from the impact velocity condition was evaluated. The geometry of the damage zone in the 304L target due to impact velocity is shown in Figure 7. Additionally, the depth and width of the hole on the front side are measured with a caliper. Enlarged views of the impact section give special attention to scanning for more than one point on that section's surface. Figure 8 shows the misorientation angle of the crater (45-55°). The plastic deformation is deformed, and the grains dislocate the plane to another plane as a twinning deformation. The following locations are selected for comparison and analysis Cross-section Location 1-C (75 mm from impact center): In this site sample 75 mm away from the crater, the 304L steel in this site was not affected, phase crystalline stayed the same, and did not show any sign of the formation of the plastic or twinning. Figure-8 shows

the EBSD microscopy data for location 1-C in the 304L steel target after an impact velocity of 6.58 km/sec. The figure shows the polished sample, grain, 400X magnification, the map's original length, and the phase distribution.

Cross-section Location 6-A (0 mm from impact center): Figure-9 shows the EBSD microscopy data for location 6-A in the 304L steel target after an impact velocity of 6.58 km/sec. The figure shows the polished sample, grain, 400X magnification, the map's original length, and the phase distribution. Although the location is close to the arc shot vicinity, the image of the EBSD microscope became apparent and did not show any change in the particle size or the presence of any form of plastically. This behavior means that the alloy was not affected by the shock under a high temperature and a high pressure.

Cross-section Location 6-B (0 mm from impact center): Figure-10 shows the EBSD microscopy data for location 3-A in 304L steel target after an impact velocity of 6.58 km/sec. The figure shows the polished sample, grain, 400X magnification, the map's original length, and the phase distribution. Table 4.9 lists the Impact phase ratios of 304L steel at 6.58 km/sec sample location 6-B.

Cross-section Location 6-C (0 mm from impact center): Figure-11 shows the EBSD microscopy data for location 6-C in 304L steel target after an impact velocity of 6.58 km/sec. The figure shows the polished sample, grain, 400X magnification, the map's original length, and the phase distribution. Under this high impact speed, no significant or dramatic changes occurred post- impact 304L steel.

Cross-section Location 6-E (0 mm from impact center): Figure-12 shows the EBSD microscopy data for location 6-E in the 304L steel target after an impact velocity of 6.58 km/sec. The figure shows the polished sample, grain, 400X magnification, the map's original length, and the phase distribution. No significant or dramatic changes occurred post-impact 304L steel under this high impact speed. Although the lowest impact affected A36 steel, let alone an even more effect on the HY100 steel, the existence of FCC having a high percentage significantly have affected the results. Before impact (BCC and FCC), since FCC is a transitional phase before transfer and reaches the hexagonal HCP phase. This is why the percentage of FCC is high through all locations of samples of 304L. The selection sample 6 locations C is a low percentage of error and higher confidence, as illustrated and discussed in chapters 6 and 7.

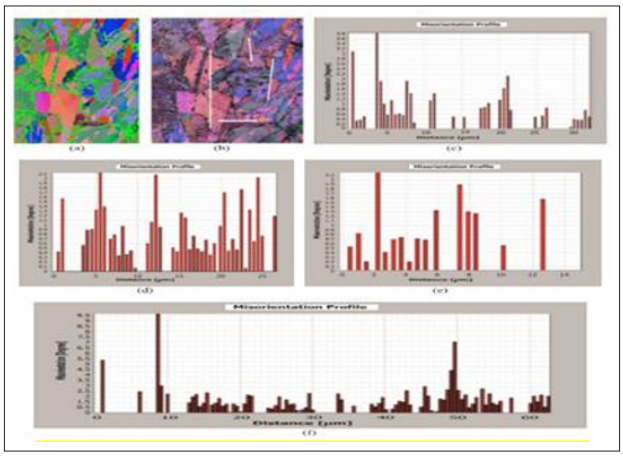

Figure 28: Misorientation angle measured along four different lines in the impacted 304L steel, sample location 6-A after impact velocity of 6.58 km/sec shows: a) EBSD shows less noise, b) EBSD shows grains, c, d, e, and f are the Lines (1, 2, 3, and 4) respectively.

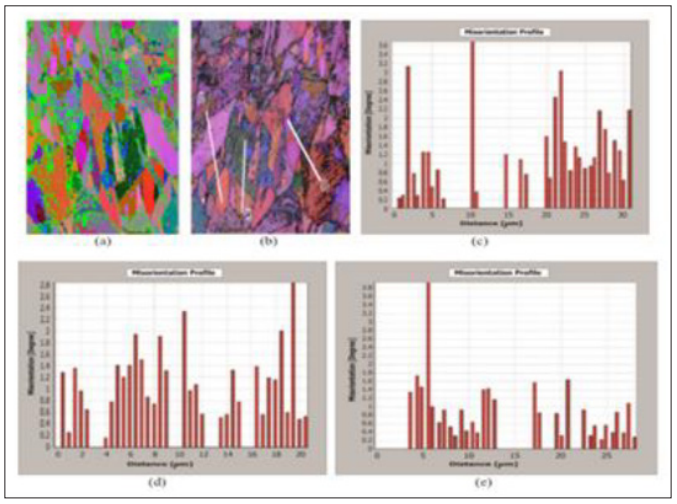

Figure 29: Misorientation angle measured along four different lines in the impacted 304L steel, sample location 6-B after impact velocity of 6.58 km/sec shows: a) EBSD shows less noise, b) EBSD grains, c) Line 1, d) Line 2, and e) Line 3.

The actual phase for this type of steel is BCC and FCC. The high speed of A36 steel (source?) had the most significant share in the emergence of phase change HCP and twinning deformation, and therefore the best option is to find the effect of a high speed of 6.58 km / s on 304L. Of all the results stated above in the tables and images as shown here of this iron alloy type, this type of steel 304L does not change its crystalline phase during impact shock under high temperatures and pressure. This phenomenon is because this type of alloy has the initial phase before impacting BCC and FCC since FCC is the transitional first phase to reach the hexagonal HCP phase. So, the percentage of FCC is high throughout all locations and samples of 304L. The grained stability on the crystalline level did not exceed the plastic limits or twinning deformation crystalline. This stability shows that this kind of Iron alloy shocked unimpaired under high pressure, and the temperature has been the crater area test and near crack figures as shown in figure- 9.

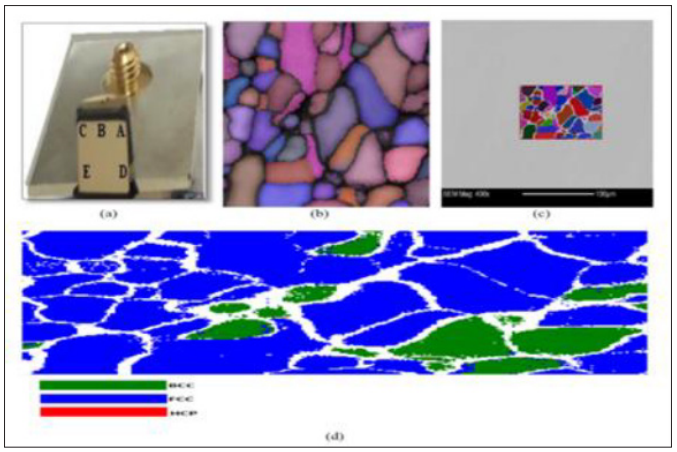

Figure 30: EBSD data from 304L steel, sample location 1-C, after impact velocity of 6.58 km/sec showing: a) polished sample, b) grain, c) 400X magnification and the original length of the map, and d) phase map.

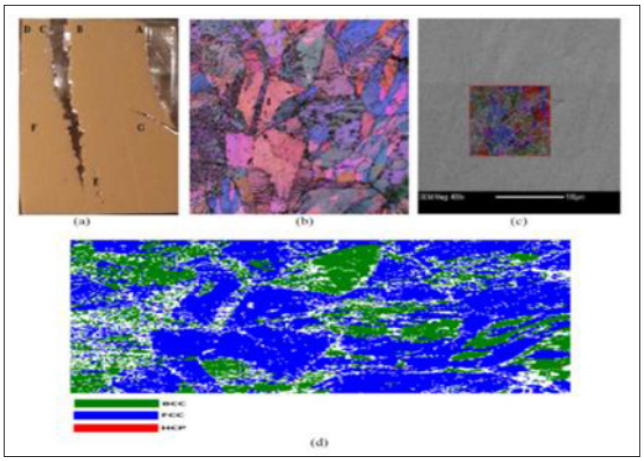

Figure 31: EBSD data from 304L steel, sample location 6-A, after impact velocity of 6.58 km/sec showing: a) polished sample, b) grain, c) 400X magnification and the original length of the map, and d) phase map.

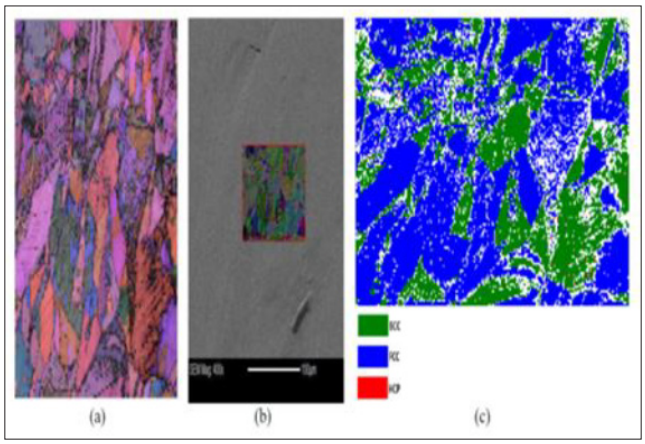

Figure 32: EBSD data from 304L steel, sample location 6-B, after impact velocity of 6.58 km/sec showing: a) grain, b) 400X magnification and the original length of the map, and c) phase map

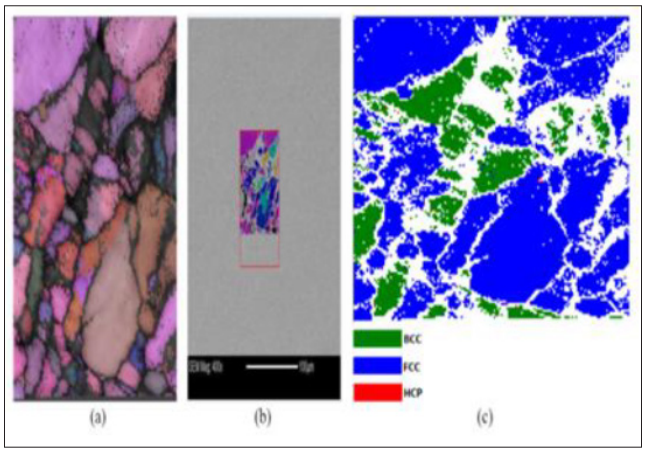

Figure 33: EBSD data from 304L steel, sample location 6-C after impact velocity of 6.58 km/sec showing: a) grain, b) 400X magnification and the original length of the map, and c) phase map.

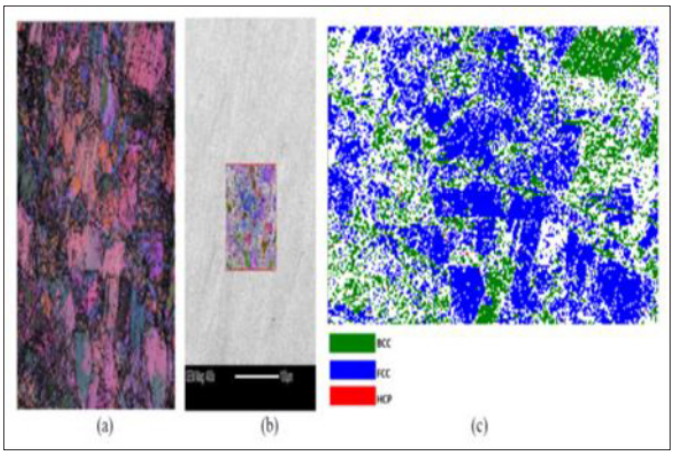

Figure 34: EBSD data from304L steel, sample location 6-E, after impact velocity of 6.58 km/sec showing: a) grain, b) 400X magnification and the original length of the map, and c) phase map

Throughout the results, images and tables indicate that 304L steel is slightly changed due to impact. Some steel's crystal phase is changed from BCC or FCC to HCP. It is well known The presence of HCP proves that the phase crystal has changed, and plastic deformation and twinning start forming on the grains' plane. They left the plane near the crater's arc and altered the BCC, HCP, or FCC crystal phase. The crystalline system remained organized. Among other things that were not observable due to the microscope's possibility of reading the arc crater's immediate area, the results in those areas deviated and cannot be relied upon.

FCC existed with insignificance pre-impact and became significant post-impact at the point of impact and the surrounding areas. However, this occurred with a lower percentage and became insignificant again away from the point of impact. The EBSD imaging samples (post-impact) observed that the grain size significantly decreased closer to the impact area (Arc of the projectile) plane that EBSD cannot scan. This area's error was so high and confidence so little, as shown at location A1, so the result is the average area. From the above figures and diagram, it is evident that the non-impacted zone does not have any HCP or a significant amount of FCC, increasing impact momentum increased the HCP Percentage, and near the crater, the HCP is higher percentile than in a region farther away.

Grain size near impact is compacted near the impact site. A light gas gun uses a gunpowder hole to fire a plastic piston into a pump tube filled with helium or hydrogen. The diluted gas is compressed as the piston moves through the pump tube. The petal valve separates the light gas from the release tube under high pressure. Deformation, which consists of slipping and twinning, is highly inelastic. At this point, it has become dominant and irreversible.

While examining 304L steel-post impact, the effects were visible to the naked eye, but the microstructure was also significantly changed. One observation was 'twinning.' twinning was present closer to the impact area and gradually dissipated further from the impact zone. Twinning was most significant during the testing of the samples from the 6.7 km per second speed impact. Another observation of the samples from the EBSD imaging (post-impact) was that the grain size significantly decreased closer to the impact area. Further away from the impact area, the grain size was less affected and resembled pre-impact sizes. It was also discovered that the higher speed impact samples showed more evidence of a

reduction in grain size than in the slower speed impact samples [16].

Misorientation is calculated from one orientation's product (or composition) and the other's inverse. Figures(8-12) show the angle phase crystalline transition in the grain boundaries of non-impact 304L steel. The raw material is stable and precise, and the prominent grain of the misorientation angle in crystals is small.

Discussion

EBSD results of 304L steel plate show two phases, BCC and FCC, co-exist in their microstructure, both in significant amounts, yet with a trace of HCP with the non-impact ratios of 33.109 %, 66.718 %, and 0.1724 %. This result shows that the main phase contents of this kind of steel are BCC and FCC.

Post-impact examination of the 304L steel cross-sections samples 1 to 6 shows the percentage values of HCP were, in sequence, 0.0188 %, 0.1225 %, 0.221 %, 0.281 %, 1.6445 and 1.699 %, with an estimation error of less than 10 % as shown in Table 6.7. One test location point was selected about 2000 microns away from the edge of impact. Analyzing the EBSD test results showed that this type of steel 304L does not change its crystalline phase during impact shock under a high temperature and pressure. This type of alloy already has a significant amount of FCC phase combined with the original BCC that exists in the pre-impact test. FCC is a transitional phase pre-formed to the hexagonal HCP phase. This explains that the high percentage of FCC throughout all test point locations for the 304L steel and the phase alteration did not exceed the plastic limits or twinning deformation. Grains in this alloy are obviously more stable at the crystalline level. These iron alloys show resistance to phase changes behavior under high pressure shocks even close to the crater and impact holes, as shown in the above Figures.

At cross-section number 6, at the impact site, selected point C, at 1000 micron from the hole's edge, shows an insignificant value of HCP 0.092 % and 9.17 % accuracy. The location test of point A result has been ignored, which shows a low confidence error of more than 20 % and an HCP percentage of 1.699 %, which is less reliable than point C, as shown in Figure-13.

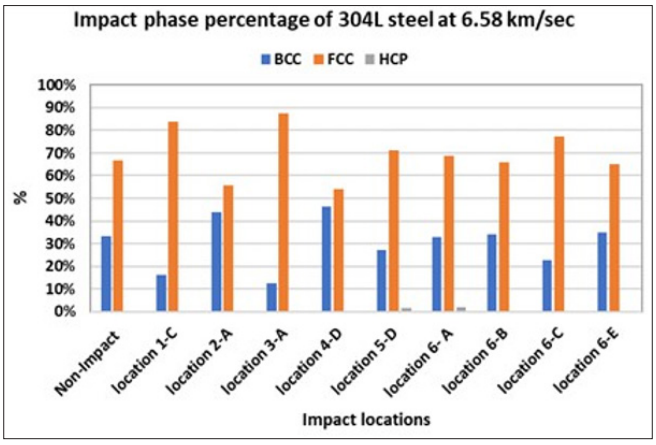

Figure 35: Impact phase percentage of 304L steel at 6.58 km/sec vs. all sample locations

More research is needed to examine different orientations to observe how twinning is formed concerning the impact area. Observing different orientations should also provide further insight into the decreasing grain size around the immediate impact area. Another point of interest would be to test hardness, pre-and post-impact, to examine the material's behavior change. The presence of HCP (post-impact) leads to the probable conclusion of an increase in brittleness.

The preliminary results and post-impact observations beyond 13 GPa, sub-structural evolution, and mechanical behavior of 304L steel agree with many types of research on similar experimental after-shock data on similar iron and alloys, such as in Gray, Hayes, and Hixon [4]. HY 100 steel EBSD has been used to examine the impacted samples in one suggested impact speed. Figure 3 shows a cross-section view of an impacted specimen. The picture indicates the crack area and what to consider the immediate impact region: otherwise, regions are designated as distant spots. Examination of the prepared samples in the study depended on two kinds of microscopy: EBSD, which is used to find the unit cell of the crystal system and determine the phase percentage with a microstructure map of the grain and phase, and XRD, which can measure the distance between the lattice parallel surfaces. This distance is defined as the lattice constant (d) [3].

Non- Impact EBSD Grain Structure View

The images shown in Figure 6, obtained from EBSD microscopy, show the grain structure of HY-100 steel that has not been impacted. Figure 6 also indicates three views that explain grain, the 350X magnification, and the map and phase's original length. Table 2 lists non-impact material phase ratios. Transition and change locations of the grains inside the crystal of non-impact HY100 are examined. Before the shock, the angle ranging is (0-4.5) ° because the crystal system and stable raw material were not exposed to any load.

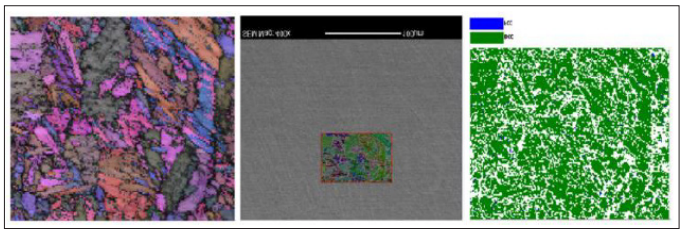

Figurer 34: Non –Impact microstructure photo on EBSD

Table 11: Non- Impact phase ratio of HY100 Steel

Crystal unit cell structures	HY100 Steel non-impact material phase %
BCC	99.78%
FCC	0.22%
HCP	0%

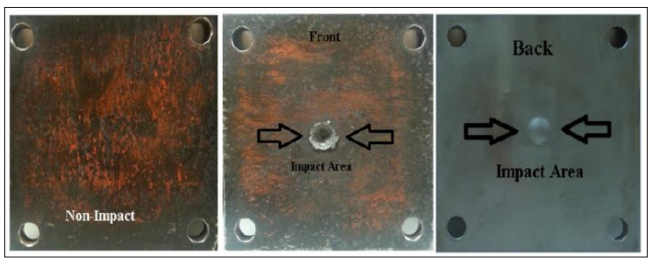

Figure 37: Non-Impacted HY100 Steel and Impact at 6.70 km/sec and sections of locations

HY-100 Steel (Impact Velocity of 6.7 Km/s)

One HY-100 target plate from the impact velocity condition was evaluated. The geometry of the damage zone in the HY-100 target due to impact velocity is shown in Figure 7. Additionally, the depth and width of the hole on the front side are measured with a caliper. Enlarged views of the impact section give special attention in scanning for more than one point on that section's surface. Figure 8 shows the misorientation angle of the crater between 55-60°. The plastic deformation is deformed, and the grains dislocate the plane to another plane as a twinning deformation.

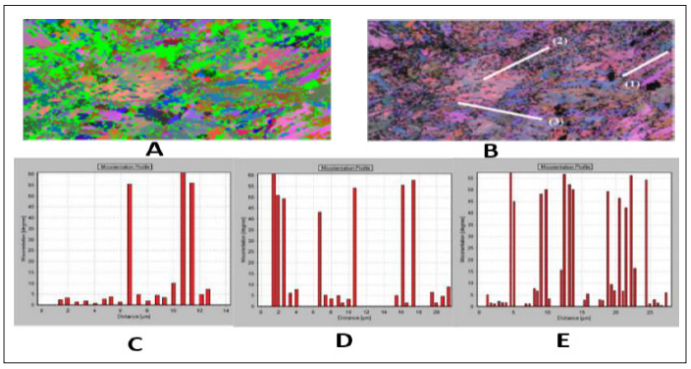

Figure 38: Impact HY100 Steel at 6.70 km/sec EBSD viewing less noise and EBSD considering grains. Lines (1, 2, 3) in sample (6) location B are grains misorientation at angle (0-60) degree twinning.

Sample 6 location C is another location at the crater sample. The misorientation angle is (55-60) degree that means the plastic deformation as a twinning is so evident in this location and HCP percentage increase. The Misorientation angle in sample (6) location E is between 55-600, and the HCP phase ratio increase. Twining deformation appeared permeant and not naturally reversible in the sample 6 location F location since a long time elapsed between experiment and EPSD viewing. Conceptually, during deformation, atoms can be pushed out of place. The Misorientation angle in the sample 6 location G location is between 55-60 degrees and the HCP phase ratio increases.

The results of HY100 Steel this kind of alloys the phase changes during the impact of high pressure and temperature and note that the crystal and grains are shaped to form a new HCP and twinning deformation leave the plane exhibition shock away. As well as the angle of misorientation, it is greater than 45 degrees. This means the grains of the crystal changed the direction and shape of the impact of the shock.

In XRD Lattice Parameter Measurements, The HY100 steel is the only sample that shows no change from non-impact to impact. Only the BCC phase is seen. It is important to note that other steel phases are not visible in the XRD data. Indeed, Throughout the results, images and tables indicate that HY 100 Steel is changed due to impact. Some steel's crystal phase is changed from BCC to FCC and HCP. The presence of HCP proves that the phase crystal has changed, and plastic deformation and twinning start forming on the grains' plane. They left the plane near the crater's arc and altered the BCC, HCP, or FCC crystal phase. The crystalline system remained organized. Among other things that were not observable due to the microscope's possibility of reading the arc crater's immediate area, making the results in those areas deviated and cannot be relied upon. Sample G is selected because the low percentage of error and higher confidence has been illustrated.

Figure 9 shows four different slides for EBSD views of the designated value. Notice the apparent twining traces in the region near the crater site. Some minor twinning appears on slide A4 and is almost null on other slides. The percentages of crystal modes for an impact speed of 6.7 Km/s are tabulated in Table 3. Figure 9 is a qualitative model showing the trend of twinning change. The most intense twinning region is around the shock center. Quantitatively, Table 3 indicates the phase mix relationship ratios and offers BCC's estimation as the dominant phase pre-impact, remaining so after impact in all slides. However, HCP started to appear near the point of impact and existed in remote locations but insignificant.

electron backscatter diffraction (EBSD) data indicate the presence of a hexagonal close-packed (HCP) phase on the impacted steels, as well as the FCC phase on the HY100. A likely reason for this discrepancy is outlined above - the "invisible" phases are not sufficiently abundant to be detected by powder XRD.

At Cross-section Location 6-A (0 mm from impact center), a small-grained size starts in the surrounding area arc crater due to the shock under the temperature and high-pressure. The error rate in this region high in the calculations was taken of the average of these areas. The best location is chosen to view EBSD microscopy images is shown in figure 9.

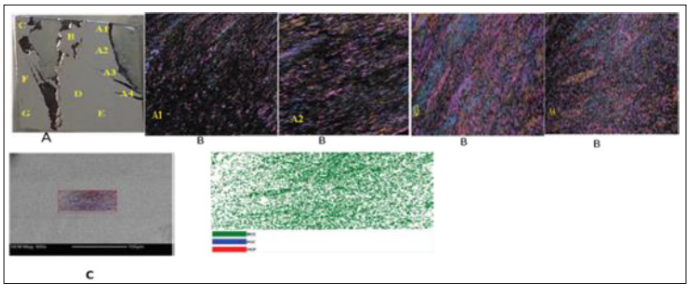

Figure 35: HY100 Steel sample (6) location A impact at 6.70 km/sec microstructure photo on EBSD.A) the Sample and locations, B) grain at four locations, C) 400X magnification and the original length of the map, and D) the Phases.

FCC existed with insignificance pre-impact and became significant post-impact at the point of impact and the surrounding areas. However, this occurred with a lower percentage and became insignificant again away from the point of impact. The EBSD imaging samples (post-impact) observed that the grain size significantly decreased closer to the impact area (Arc of the projectile) plane that EBSD cannot scan. This area's error was so high and confidence so little, as shown at location A1, so the result is the average area.

Figure 9 is qualitative and shows the trend of twinning change. The tensest twinning region is around the shock center. HCP started to appear near impact and existed in the distant locations but with an insignificant proportion. FCC existed with insignificant pre-impact and became significant after impact at the impact and the neighborhood near impact, however witt lower percentage and became insignificant again away for impact. From the above figures and diagram, it is evident that:

- The non-impacted zone does not have any HCP or a significant amount of FCC
- Increasing impact momentum increased the HCP Percentage.
- Near the crater, the HCP is higher percentile than in a region farther away.

Grain size near impact is compacted near the impact site. A light gas gun uses a gunpowder hole to fire a plastic piston into a pump tube filled with helium or hydrogen. The diluted gas is compressed as the piston moves through the pump tube. The petal valve separates the light gas from the release tube, which is located under high pressure. Deformation, which consists of slipping and twinning, is highly inelastic. At this point, it has become dominant and irreversible. While examining HY-100 steel-post impact, not only were the effects visible to the naked eye, but the microstructure was also significantly changed. One observation was 'twinning.' twinning was present closer to the impact area and gradually dissipated away further from the impact zone. More twinning was present in the higher speed impact samples than the lower speed impact samples. Twinning was most significant during the testing of the samples from the 6.7 km per second speed impact.

Another observation of the samples from the EBSD imaging (post-impact) was that the grain size significantly decreased closer to the impact area. Further away from the impact area, the grain size was less affected and resembled pre-impact sizes. It was also discovered that the higher speed impact samples showed more evidence of a reduction in grain size than in the slower speed impact samples [15].

More research is needed to examine different orientations to observe how twinning is formed concerning the impact area. Observing different orientations will also provide further insight into the decreasing grain size around the immediate impact area. Another point of interest would be to test hardness, pre-and post-impact, to examine the material's behavior change. The presence of HCP (post-impact) leads to the probable conclusion of an increase in brittleness. The preliminary results and post-impact observations beyond 13 GPa, sub- structural evolution, and mechanical behavior of HY- 100 steel agree with many types of research on similar experimental after-shock data on similar iron and alloys, such as in Gray, Hayes, and Hixon [4].

Regarding orientation and rotation, additional evidence of twinning in the examined samples by the EBSD has been tabulated As in phase-ratio changes. When the changes in the misorientation profile range from 55 to 60 degrees in a range of .02 mm length between two points, this is clear evidence of the existence of twinning. Conversely, a change of the order of 0.1 to 3.0 degrees indicates no twinning deformation.

Misorientation is calculated from the product (or composition) of one orientation and the other's inverse. Figure 9 shows the angle phase crystalline transition in the grain boundaries of non-impact HY- 100 steel. The raw material is stable and precise, and the prominent grain of the misorientation angle is in tiny crystals ranging from 0-1.60°. The misorientation angles at 3mm, far from the projectile's impact arc. The HCP phase in this location increased. Twinning was also noted to have risen- all lines show that the new deformation starts here and changes the BCC phase to FCC and HCP.

Discussion

Pre-impact EBSD show relatable test results value of 0.002-FCC and 99.98 BCC, and null-HCP in HY 100 steel. Post-Impact HY 100 steel test results of 6.70 km/sec, the percentage of HCP ratio for the cross-signal section sample l to 5 to be, in order, (0.31, 0.373, 0.40, 1.12 and 1.50)%. As for the cross-section sample 6, at impact section, the percentage of HCP is around 2.29 percent at point G, taken as a reliable comparing point located at 2000 micron near crated and projectile hole edge, its error is acceptable at 9.15 percent. Estimation certainty at this point is over 90 percent. Other points located at the same cross-section 6 are A, B, C, gage value of HCP: l.432, 2.50, and 2.29%, with reasonable confidence. The crystal phase change from BCC to FCC and HCP in this kind of steel compared to the 304L. EBSD results for HY 100 steel post-impact test prove that the microstructure phase has changed. Plastic, twinning, and plastic deformation start forming on the plane of the grains near arc and crater of crater section from body-centered cubic (BCC) into a hexagonal close-packed (HCP) and face-centered cubic (FCC). Also, Figures and tables show that misorientation angles of more than 45 degrees. This means the crystal grains have changed the direction and shape due to shock impact. EBSD reading results of the arc crater's immediate area are very dull and dark and reflect very high error, making the results in those areas inaccurate and unreliable.

As for the HY100 steel test result shown in table 3, HY100 steel has the original phase BCC and the percentage is 99.78% and FCC 0.22%. After impact, the phase change and the HCP phase increase and BCC decrease and some percentage of FCC a transmission phase 97.32%, 0.391%, and 2.29%.

At 6.70 km/sec at location A, the error was 3.91%, and the proportion of reliability 96.09%. This point location was the crater's areas carrying hexagonal crystalline phase and the ratio of the misorientation angle of (50 - 60) degree, which implies occurrence.

The HY100 steel scanning shows HGP percentage at the section sample 1 to 5 to be (0.31, 0.373, 0.40, 1.12, and 1.342), with high accuracy estimate. In section sample 6, impact area, the HCP percentage was around (1.432, 2.50, and 2.29) %.

Table 12: The Ratio of All Phases Depending on Cratering Location HY100 Steel at 6.70 km/sec

Section Samples Numbers	crystal unit cell structures	Impact HY 100 Steel Phase at 6.70 km/sec
Sample 1	BCC	99.55%
	FCC	l.l4l%
	HCP	0.3l%
Sample 2	BCC	98.03%
	FCC	l.598%
	HCP	0.373%
Sample 3	BCC	97.742%
	FCC	l.866%
	HCP	0.40%
Sample 4	BCC	98.l8%
	FCC	0.7l%
	HCP	l.l2%
Sample 5	BCC	97.70%
	FCC	0.804%
	HCP	l.50%
Sample 6 Location A	BCC	97.32%
	FCC	0.39l%
	HCP	2.29%

Non-Impact HY100 Steel Phase	BCC	99.78%
	FCC	0.22%
	HCP	0%

Conclusion

A36

As Gray, Hayes, and Hixon had indicated, in the shock propagation in Fe BCC-HCP transient front was quenched by the rarefaction release producing a gradient in shock hardening which is a function of propagation distance [1]. A post-impact study of A36 steel would verify the finding in future work. The effect of impact upon surface hardness may be examined.

More research is needed concerning examining the presence of twin phases in some of the images and why they appear in specific test locations. Imaging also needs to be improved, especially pertaining to grain size. Additionally, according to previous publication in the fields, iron may be transformed into stable and metastable non- BCC phases by manipulation of thermodynamic parameters. These facts may be verified in more experiments. It should be considered that the low percentage of HCP is possibly a result of the noise level of the system. Additional statistical analysis is needed to determine the confidence level intervals of the calculated rates. Alternately, ion polishing could be used to improve the image quality of the 'near zone' post-impact, especially for the 5.80 km/per second-speed impact samples, since more accurate viewing is needed to recover details of the site near the crater. This process would allow different projectile materials and shapes to be used.

Next paper will focus on our XRD results. The EBSD was capable of mapping grain boundary (X=400), surrounding grains, (boundary condition (BC) and boundary grain (BG) (X=400), ratio of the phase percentage and the error, Crystal Orientation Magnification, and the original length of the map and Misorientation angle greater than 45° having twinning. However, EBSD was not capable of estimating changes in lattice constants and physical properties, mass, volume, density, and grain size.

Although the focus in this article is the A36 steel, in future publications, we ought to compare the effect of high-energy impact on other iron metals in terms of substructure changes.

304L

The 304L steel show has three phases: BCC, FCC, and some small percentage of HCP 33.109 %, 66.718%, and 0.1724 %, respectively. The real phase of this kind of steel is BCC and FCC. In this kind of steel, the choice is only one high-speed impact of 6.58 km/sec, and after that, it was found that the high speed of A36 steel has had the biggest share of the appearance of change-phase HCP and twining deformation. For the 304L steel, the percentage of HCP ratio is at the section's samples 1 to 6, 0.0188 %, 0.1225 %, 0.221%, 0.281 %, 1.6445 % and 1.699 %. Of all the results stated above in the tables and images of this iron alloy type, this type of steel 304L does not change its crystalline phase during impact shock under high temperatures and pressure. This type of alloy has the initial phase before impacting BCC and FCC since FCC is the transitional first phase to reach the hexagonal HCP phase. This is why the percentage of FCC is high throughout all locations and samples of 304L. The grained stability on the crystalline level did not exceed the plastic limits or twinning deformation crystalline. This shows that this kind of Iron alloy shocked unimpaired under high pressure, and the temperature has been the crater area test and near crack.

HY 100

This work shows that HY 100 Steel has changed the crystal phase from BCC to FCC and HCP and that plastic deformation and twinning start forming. The change partially occurred from (BCC) into (HCP), or (FCC). Also, misorientation had appeared greater than 45 degrees. This means the grain size of the crystal changed the direction due to the shock impact.

The shock propagation in the Fe BCC-HCP transient front was quenched by the rarefaction release producing a gradient in shock hardening, which is a function of propagation distance. A post-impact study of HY-100 steel would verify the finding in future work. The effect of impact upon surface hardness may be examined.

More research is needed concerning examining the presence of twin phases in some of the images and why they appear in specific test locations. Imaging also needs to be improved, especially about grain size. Previous publications indicate that iron may transform into stable and meta-stable non-BCC phases by manipulating thermodynamic parameters. These facts may be verified in more experiments should be borne in mind that a lower HCP percentage may result from the system's noise level. Extra statistical analysis is needed to determine the confidence level intervals of the computed rates. Alternately, ion polishing could improve the image quality of the 'near zone' post- impact, especially for the 5.80 km/per second-speed impact samples, since more accurate viewing is needed to recover details of the site near the crater. This process would allow different projectile materials and shapes to be used.

The following paper will focus on our XRD results. The EBSD was capable of mapping grain boundary (X=400), surrounding grains, (boundary condition (B.C.) and boundary grain (B.G.) (X=400), the ratio of the phase percentage and the error, Crystal Orientation Magnification, and the original length of the map and Misorientation angle greater than 45° having twinning. However, EBSD could not estimate changes in lattice constants and physical properties, mass, volume, density, and grain size.

Although the focus in this article is the HY-100 steel, in future publications, we ought to compare the effect of high-energy impact on other iron metals in substructure changes.

Acknowledgements

A36

This work is made possible by a grant from the US Department of Energy (DOE) under Contract No. DE-AC52-06 NA25946 with National Technology Security, LLC, and the concerted efforts of the UNLV team of professors and researchers.

References

1. D GrayIII, B Haye, RS Hixon (2000) EDP sciences. Influence of the shock_iduced α-ε transition in Fe on its post-shock substructure evolution and mechanical behavior. Journal of Physics IV 10: 755-760.
2. MV Zhernokletov, BL Glushak (2007) Material Properties under Intensive Dynamic Loading. Springfield. https://link.springer.com/book/10.1007/978-3-540-36845-8.
3. LM Dougherty, GT Gray III, EK Cerreta, RJ McCabe, RD Field, et al. (2009) Rare twin-linked to high-pressure phase transition in iron. Scr. Mater 60: 772-775.
4. ASTM A36 Steel Plate (2015) O'Neal The Metals Company. Website http://www.onealsteel.com/carbon-steel-plate-a36.

html.
5. Primary Metallic Crystalline Structures (BCC, FCC, HCP) (2015) NDT Rsrcs. https://www.ndeed.org/EducationResources/CommunityCollege/Materials/Structure/met allic_structures.htm.
6. SJ Wang, ML Sui, YT Chen, QH Lu, E Ma, et al. (2013) Microstructural fingerprints of phase transitions in shock-loaded iron. Scientific Reports 3: 1086.
7. SK Saxena, LS Dubrovinsky (2000). Iron phases at high pressures and temperatures: Phase transition and melting. Am Mineral 85: 372-375.
8. Johnson GR, Cook WH (1983) A Constitutive Model and Data for Metals Subjected to Large Strains, High Strain Rates, and High Temperatures, 7th International Symposium on Ballistics, The Hague, Netherlands 541.
9. Deformation twinning (2015) University of Cambridge, Website http://www.doitpoms.ac.uk/tlplib/superelasti city/twinning.php.
10. UF Kocks, CN Tomé, HR Wenk (1998) Texture and Anisotropy: Preferred Orientations in Polycrystals and their Effect on Materials Properties, Cambridge University Press.
11. T Maitland, S Sitzman Electron Backscatter Diffraction (EBSD) Technique and Materials Characterization Examples.
12. M Slewa, BO'Toole, M Trabia (2014) Effect of High-Velocity Impact on Grain Structure of A36 Steel. Photonic Doppler Velocimetry Workshop, Las Vegas, NV 24-26.
13. S Roy, M Trabia, BO'Toole, J Thota, R Jennings, et al. (2013) Plastic Deformation of Steel Plates under High Impact Loading, Abstract, 84th Shock & Vibration Symposium, Atlanta GA 3-7.
14. M Pena, S Becker, A Garza, M Hanache, R Hixson, et al. (2015) Many Point Optical Velocimetry for Gas Gun Applications. 19th Biennial Conference on Shock Compression of Condensed Matter (SCCM-2015), American Physical Society, Tampa, FL 14-19.
15. BO'Toole, M Trabia, RJennings, S Roy, M Matthes, et al. (2015) Multiplexed Photonic Doppler Velocimetry (MPDV) Application in Plastic Deformation Experiments under Hypervelocity Condition, Photonic Doppler Velocimetry.
16. AISI Type 304L Stainless Steel, ASM Material Data Sheet (matweb.com)Part II:Bonding insolids 1 Vander Waals bonds. https://phas.ubc.ca/~berciu/TEACHING/PHYS315/L ECTURES/FILES/bonding.pdf.
17. UF Kocks, CN Tomé, HR Wenk (1998) Texture and Anisotropy: Preferred Orientations in Polycrystals and their Effect on Materials Properties, Cambridge University Press.
18. Muna Slewa (2020) Crystalline Phase Change Due to High-Speed Impact on A36 Steel, Proceedings of the ASME 2020, International Mechanical Engineering Congress and Exposition, IMECE2020, Portland, USA 15-19.
19. American Society of Mechanical Engineers - Virtual Conference Resources (secure-platform.com).
20. Muna Slewa Crystalline Phase Change in Steel Alloys due to High-Speed Impact Department of Mechanical Engineering Howard R. Hughes College of Engineering the Graduate College University of Nevada, Las Vegas December 201HY 100:
21. HY 100 Alloy Steel – UNS K32045 (2015) AZO Materials Website: http://www.doitpoms.ac.uk/tlplib/superelasticity/twinning.php http://www.azom.com/article.aspx?ArticleID=6734.
22. Zhendong Fu, Yinguo Xiao, Artem Feoktystov, Vitaliy Pipich, Marie-Sousa Appavou, et al. (2016) Field-induced self-assembly of iron oxide nanoparticles investigated using small-angle neutron scattering The Royal Society of Chemistry 2016 Nanoscale 8:18541-18550 Part II:Bonding insolids 1 Vander Waals bonds. https://phas.ubc.ca/~berciu/TEACHING/PHYS3 15/LECTURES/FILES/bonding.pdf
23. M Slewa, BO Toole, M Trabia (2014) Effect of High-Velocity Impact on Grain Structure of HY-100 Steel, Photonic Doppler Velocimetry Workshop, Las Vegas, NV 24-26.